nature immunology

ARTICLES

https://doi.org/10.1038/s41590-022-01200-7

Single-cell analysis identifies the interaction of altered renal tubules with basophils orchestrating kidney fibrosis

Tomohito Doke[1], Amin Abedini[1], Daniel L. Aldridge[2], Ya-Wen Yang[1], Jihwan Park[1], Christina M. Hernandez[3], Michael S. Balzer[1], Rojesh Shrestra[1], Gaia Coppock[1,2], Juan M. Inclan Rico[3], Seung Yub Han[4], Junhyong Kim[4], Sheng Xin[1], Adrian M. Piliponsky[5], Marco Angelozzi[6], Veronique Lefebvre[6], Mark C. Siracusa[3], Christopher A. Hunter[2] and Katalin Susztak[1]✉

Inflammation is an important component of fibrosis but immune processes that orchestrate kidney fibrosis are not well understood. Here we apply single-cell sequencing to a mouse model of kidney fibrosis. We identify a subset of kidney tubule cells with a profibrotic-inflammatory phenotype characterized by the expression of cytokines and chemokines associated with immune cell recruitment. Receptor–ligand interaction analysis and experimental validation indicate that CXCL1 secreted by profibrotic tubules recruits CXCR2$^+$ basophils. In mice, these basophils are an important source of interleukin-6 and recruitment of the T_H17 subset of helper T cells. Genetic deletion or antibody-based depletion of basophils results in reduced renal fibrosis. Human kidney single-cell, bulk gene expression and immunostaining validate a function for basophils in patients with kidney fibrosis. Collectively, these studies identify basophils as contributors to the development of renal fibrosis and suggest that targeting these cells might be a useful clinical strategy to manage chronic kidney disease.

Fibrosis is the result of chronic inflammatory reactions induced by a variety of stimuli, including persistent infections, autoimmune reactions, allergic responses, chemical insults, radiation and tissue injury[1]. Renal fibrosis, the manifestation of chronic kidney disease (CKD) is the final pathway for end-stage renal failure. Overall, 850 million people suffer from CKD and its incidence is increasing[2]. CKD is one of the fastest-growing causes of death but treatment options are limited. Gaining a better understanding of the mechanism that regulates renal fibrosis is critically important to develop new therapeutic approaches to better manage this chronic condition.

Comprehensive genome-wide human kidney tissue transcriptomics identified changes in the expression of a large number of genes in fibrosis. Differentially expressed genes (DEGs) were enriched for metabolism and proximal tubule cell changes, indicating tubule cell dysfunction and loss in fibrosis[3]. As might be expected, inflammation and immune cell response signatures represented the second-largest gene cluster associated with kidney fibrosis[3]. However, a critical knowledge gap remains as the immune cells associated with kidney fibrosis have not been systematically characterized and the trigger for immune cell influx is poorly understood. Consequently, the immune cell interactions that contribute to the initiation and development of fibrotic processes in CKD are not well understood.

The activation of basophils, a rare innate immune cell type, is associated with a variety of allergic diseases[4]. Basophils respond to a wide array of stimuli including antibody–antigen complexes and cytokines such as interleukin (IL)-3, IL-18 and IL-33. Once activated, basophils release mediators of inflammation, including histamine, leukotrienes, prostaglandins, cytokines (IL-3, IL-4, IL-6, IL-9 and IL-13) and chemokines (CCL3 and CCL4)[5]. In addition to their effector functions, basophils have been shown to influence other immune cells such as macrophages and lymphocytes[6,7]. Basophils have been implicated in immune-mediated kidney disorders[8]; however, their role in kidney fibrosis remains to be defined. Exploring the role of basophils in renal fibrosis is rational and attractive considering recent reports demonstrating an association between basophils and cardiac allograft fibrosis[9] and myocardial infarction[10].

Mast cells were once thought to be basophils that migrated from the blood into their resident tissues, but they are now known to be distinct cell types[11]. In contrast to basophils, mast cells have been proposed to play important role in CKD and renal fibrosis[12].

To unravel the molecular mechanism of kidney fibrosis development and disentangle the immune cell network, we performed single-cell RNA sequencing (RNA-seq) and analyzed the transcriptome of over 60,000 individual cells. This strategy identified alteration in proximal tubule cells and their interaction with basophils as an unappreciated and key pathway that contributes to renal fibrosis.

Results

The cellular atlas of kidney fibrosis. To develop a comprehensive overview of the cellular and molecular changes associated with kidney fibrosis, we analyzed the transcriptome of 77,393 individual

[1]Department of Medicine, Renal Electrolyte and Hypertension Division, University of Pennsylvania, Philadelphia, PA, USA. [2]Department of Pathobiology, University of Pennsylvania School of Veterinary Medicine, Philadelphia, PA, USA. [3]Center for Immunity and Inflammation, Department of Medicine, New Jersey Medical School, Rutgers–The State University of New Jersey, Newark, NJ, USA. [4]Department of Biology, University of Pennsylvania, Philadelphia, PA, USA. [5]Center for Immunity and Immunotherapies, Seattle Children's Research Institute, Seattle, WA, USA. [6]Division of Orthopaedic Surgery, Department of Surgery, The Children's Hospital of Philadelphia, Philadelphia, PA, USA. ✉e-mail: ksusztak@pennmedicine.upenn.edu

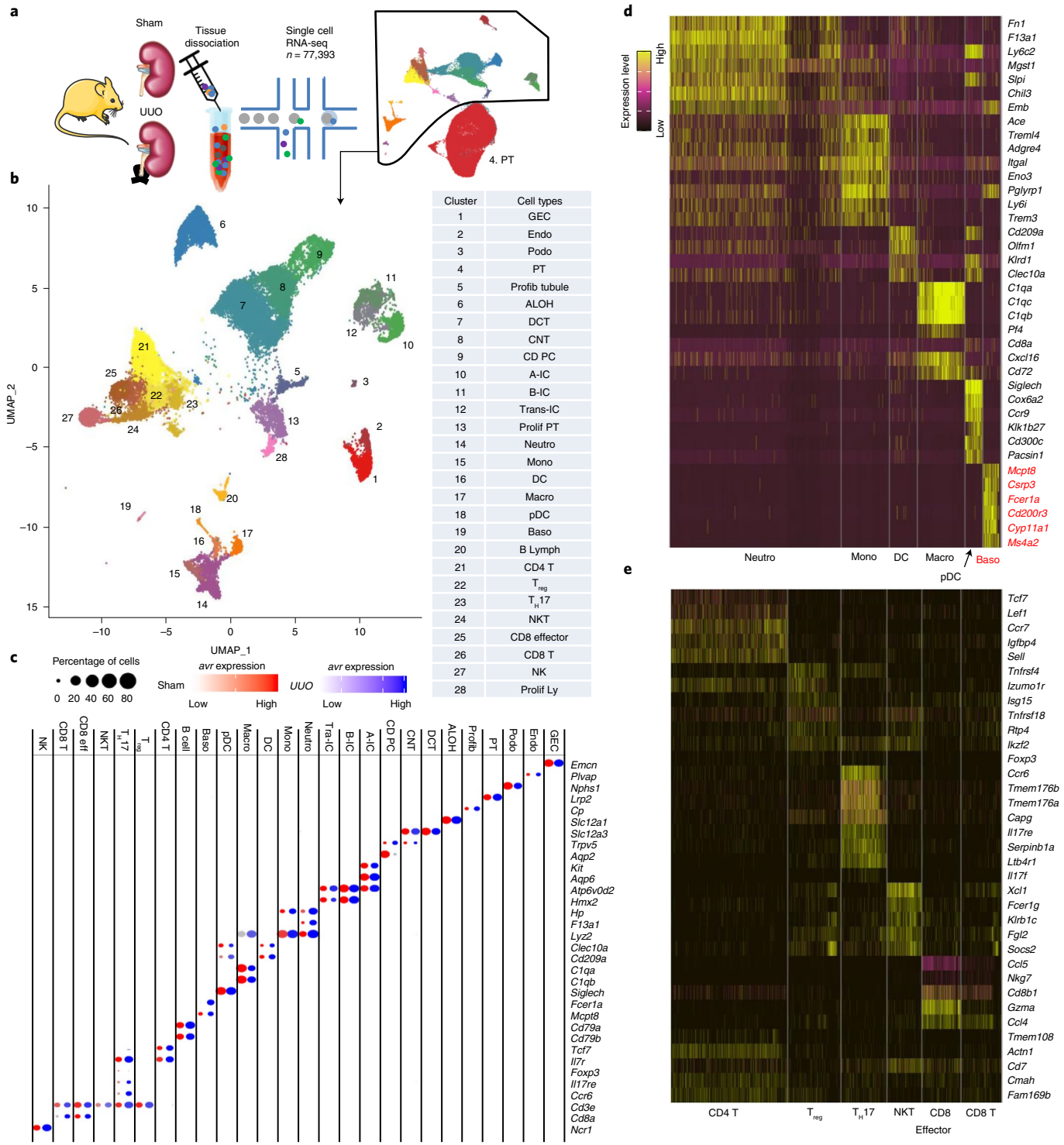

Fig. 1 | Single-cell atlas of mouse kidney fibrosis. a, Experimental procedure. Kidneys from six sham and two UUO wild-type (WT) mice were digested into single cells and subjected to single-cell RNA-seq using 10X Genomics. **b**, Uniform Manifold Approximation and Projection (UMAP) dimension reduction of 59,609 cells showing 28 distinct cell types identified by unsupervised clustering. GEC, glomerular endothelial cell; Endo, endothelial; Podo, podocyte; Profib, profibrotic; ALOH, ascending loop of Henle; DCT, distal convoluted tubule; CNT, connecting tubule; CD PC, collecting duct principal cell; A-IC, α intercalated cell; B-IC, β intercalated cell; Trans-IC, transitional intercalated cell; Prolif PT, proliferating PT; Neutro, neutrophil; Mono, monocyte; Macro, macrophage; Baso, basophil; B Lymph, B lymphocyte; Prolif Ly, proliferating lymphocyte. **c**, Bubble plots showing the expression of cell cluster marker genes in sham (red) and UUO kidneys (blue). **d**, Heat map showing gene expression patterns in myeloid cells (Neutro, Mono, DC, Macro, pDC and Baso). Each row represents one gene and each column represents a cell. Genes enriched in the basophil cluster were highlighted in red. **e**, Heat map showing gene expression patterns in lymphoid cells ($CD4^+$, T_{reg}, T_H17, NKT, $CD8^+$ effector and $CD8^+$ T). Each row represents one gene and each column represents a cell.

cells from kidneys of wild-type mice subjected to sham or unilateral ureter obstruction (UUO) surgery (six kidneys from sham and two kidneys from UUO; 31,323 cells from sham and 46,070 cells from UUO; Fig. 1a). After initial dimension reduction, we excluded proximal tubules (PTs) (as they represented the majority of cells) to accurately cluster smaller cell populations. Unbiased clustering identified 28 cell populations (Fig. 1b). Cell clusters were annotated based on previously reported marker gene expression and identified kidney epithelial cells, including podocytes, epithelial cells from different tubule segments and immune cell populations that included different T cell populations and a variety of innate cell types (Fig. 1b, Supplementary Figs. 1 and 2 and Supplementary Table 1). Fibroblasts were part of cluster 2 (endothelial cells) and showed enrichment for classic fibroblast markers such as *Col1a1*, *Col3a1*, *Dcn* and *Pdgfrb*[13,14] (Supplementary Fig. 3). Key cell type-specific markers were preserved in fibrotic samples and could be used to accurately identify cell types both in sham and UUO samples (Fig. 1c). As immune cells are often difficult to distinguish only based on gene expression information, reference gene expression datasets generated for sorted cells by the ImmGen database[15] were leveraged. This approach revealed the presence of six different myeloid cells such as neutrophils, monocytes, macrophages, dendritic cells (DCs), plasmacytoid dendritic cells (pDCs) and basophils. For instance, we identified pDCs by the expression of *Siglech*, *Cox6a2* and *Cd300c* in cluster 18 (Fig. 1d). These markers can specifically identify pDCs even when more than 200 immune cell types were profiled (Supplementary Fig. 4a,b). The reference datasets also allowed us to identify DCs and macrophages. Basophils were identified based on their expression of *Mcpt8*, *Fcer1a* and *Cd200r3* (Fig. 1d and Supplementary Fig. 4a,b). Basophils did not express neutrophil (*S100a8*), eosinophil (*Il5ra* and *Siglecf*) and mast cell (*Mcpt4* and *Kit*) markers (Extended Data Fig. 1a). The presence of *Mcpt8*-positive basophils in kidneys of UUO or folic acid injection-induced fibrosis was validated by in situ hybridization (Extended Data Fig. 1b). Using the ImmGen database we also detected six different clusters of T cells; CD4$^+$ T, regulatory (T_{reg}), T_H17 subset of helper T, natural killer T (NKT), CD8$^+$ effector and CD8$^+$ T cells (Fig. 1e). The majority of immune cells were observed in UUO samples; only a few immune cells were detected in sham kidneys[16] (Supplementary Fig. 5a,b), indicating the increased immune cell number and diversity in kidneys with fibrosis. For further validation, we also integrated our results with publicly available single-cell RNA-seq data obtained from UUO kidneys (collected at different time points)[17]. The percentage of basophils in UUO kidneys were similar in both datasets, demonstrating the robustness of our analysis (Extended Data Fig. 2a–c).

The identification of profibrotic PT in kidney fibrosis. Next, we examined cell-type-specific gene expression changes in fibrotic samples. The full list of cell-type-specific gene expression differences are in Supplementary Table 2. We found that PT cells had one of the largest numbers of DEGs. Subclustering and cell trajectory analyses were performed to identify disease-specific dynamic PT cell differentiation changes in UUO kidneys. Our previous studies identified five PT subclusters: precursor, S1-precursor, two S1 clusters and S3 clusters in control healthy kidneys[3]. Subclustering of UUO PT cells identified eight PT cell types, including precursor, S1, S2 and S3 PTs (Fig. 2a and Supplementary Table 3). The analysis revealed a subcluster with high *Mki67* expression (Fig. 2b), likely representing proliferating PT cells. Notably, another subcluster expressed high levels of *Pdgfb*, well-known secreted molecules responsible for fibroblast activation[18] (Fig. 2b). We labeled these cells 'profibrotic PT' cells. Profibrotic PT cells were positive for the well-known PT cell markers *Lrp2* (encode megalin) and *Slc34a1* (refs. [19,20]), confirming that these cells are actual PT cells (Extended Data Fig. 3a).

In total, this analysis identified 404 DEGs in profibrotic PT cells (adjusted P value <0.05; Supplementary Table 3), of which 82 overlapped with the profibrotic PT cell signature characterized in our ischemic injury model (Balzer et al. under review; Extended Data Fig. 3b). It is noteworthy that profibrotic PT cells also expressed a proinflammatory gene signature that included *Cd74*, *Tnfrsf12a*, *Cxcl1*, *Cxcl10* and *Cxcl16* (Supplementary Table 3).

In addition to the profibrotic PT cell cluster, we identified an another cluster expressing a profibrotic and inflammatory gene signature such as *Pdgfb* and *Cxcl1* (cluster 5 in Figs. 1a and 2b and Supplementary Table 1). These cells expressed the tubule epithelial marker, *Epcam* and were weakly positive for PT markers *Lrp2*, *Hnf4a* and *Slc34a1*, but negative for others such as *slc13a3* and *slc22a6*. They were also positive for descending loop of Henle markers *Aqp1*, *Cryab* and *Cp*[21] (Fig. 2b and Extended Data Fig. 3a,c). The descending loop of Henle is the next tubule segment contiguous with the PT. We labeled these cells as profibrotic tubules.

To evaluate the potential origin and cellular differentiation of the profibrotic PT cluster, we performed RNA velocity analysis. Compared to the previously observed simple differentiation of precursor cells into S1 and S3 segment PT cells, we observed an alternative differentiation path from precursor PT cells toward profibrotic PT cells in UUO kidneys (Fig. 2c). Cell trajectory analysis depicted by Monocle further validated the alternative differentiation of profibrotic PT cells from precursor PT cells. Profibrotic PT cells were again enriched for the expression of a fibroinflammatory genes such as *Cxcl1*, *Cxcl10*, *Pdgfb*, *Bcl3*, *Tnfrsf12a*, *Cd74* and *Vcam1* (refs. [22,23]; Fig. 2d). Regulon activity analysis for PT subclusters identified higher expression levels of *Bcl3*, *Cebpb*, *Hes1*, *Stat3*, *Klf6*, *Stat5a* and *Ddit3*. These transcription factors are known to directly regulate cytokine expression[24] (Extended Data Fig. 4 and Supplementary Table 4).

To confirm and visualize profibrotic PT tubules, double in situ hybridization was performed in sham and UUO kidneys using probes for *Pdgfb*, *Cd74*, *Tnfrsf12a*, *Cxcl10* or *Bcl3*; markers identified in profibrotic PT cells and *Hnf4a*, the well-established PT-specific marker. Cells expressing profibrotic markers (in blue) seemed to be distributed randomly within the *Hnf4a*-positive (in pink) PTs (Fig. 2e). Their expressions were markedly higher in UUO kidneys compared to sham (Fig. 2f).

Collectively, subclustering, RNA velocity, cell trajectory, regulon activity and in situ hybridization identified profibrotic PT cells in UUO kidneys, whereas their increased expression of cytokines and chemokines suggested that they could contribute to fibro-inflammation.

Profibrotic PT recruit basophils and other immune cells. As profibrotic tubules expressed a large number of cytokines and chemokines, we explored cell–cell interactions in UUO kidneys using comprehensive receptor–ligand binding information. Particularly, we observed the expression of *Il34*, *Cxcl16* and *Cxcl10*, in profibrotic PT cells and their receptors, *Csf1r*, *Cxcr6* and *Cxcr3* in lymphoid or myeloid cells, respectively (Fig. 3a). In addition, profibrotic PT cells expressed *Pdgfb*, a key profibrotic growth factor and its receptor, *Pdgfrb*, was expressed by fibroblasts (Fig. 3a). Together, these results suggest that profibrotic PT cells may contribute to the recruitment of myeloid and lymphoid cells and the local activation of fibroblasts[25–27]. In silico deconvolution of bulk RNA-seq data confirmed an increase in lymphoid and myeloid cells including basophils in UUO kidneys whereas the fraction of renal tubular epithelial cells was decreased (Fig. 3b).

We next focused on basophils as their role in kidney fibrosis has not been studied. First, we experimentally validated the presence and the increase in kidney basophils fraction in UUO kidneys by FACS using multiple established standard basophil markers, such as CD49b, CD200R3 and FcεR (Fig. 3c and Supplementary Fig. 6).

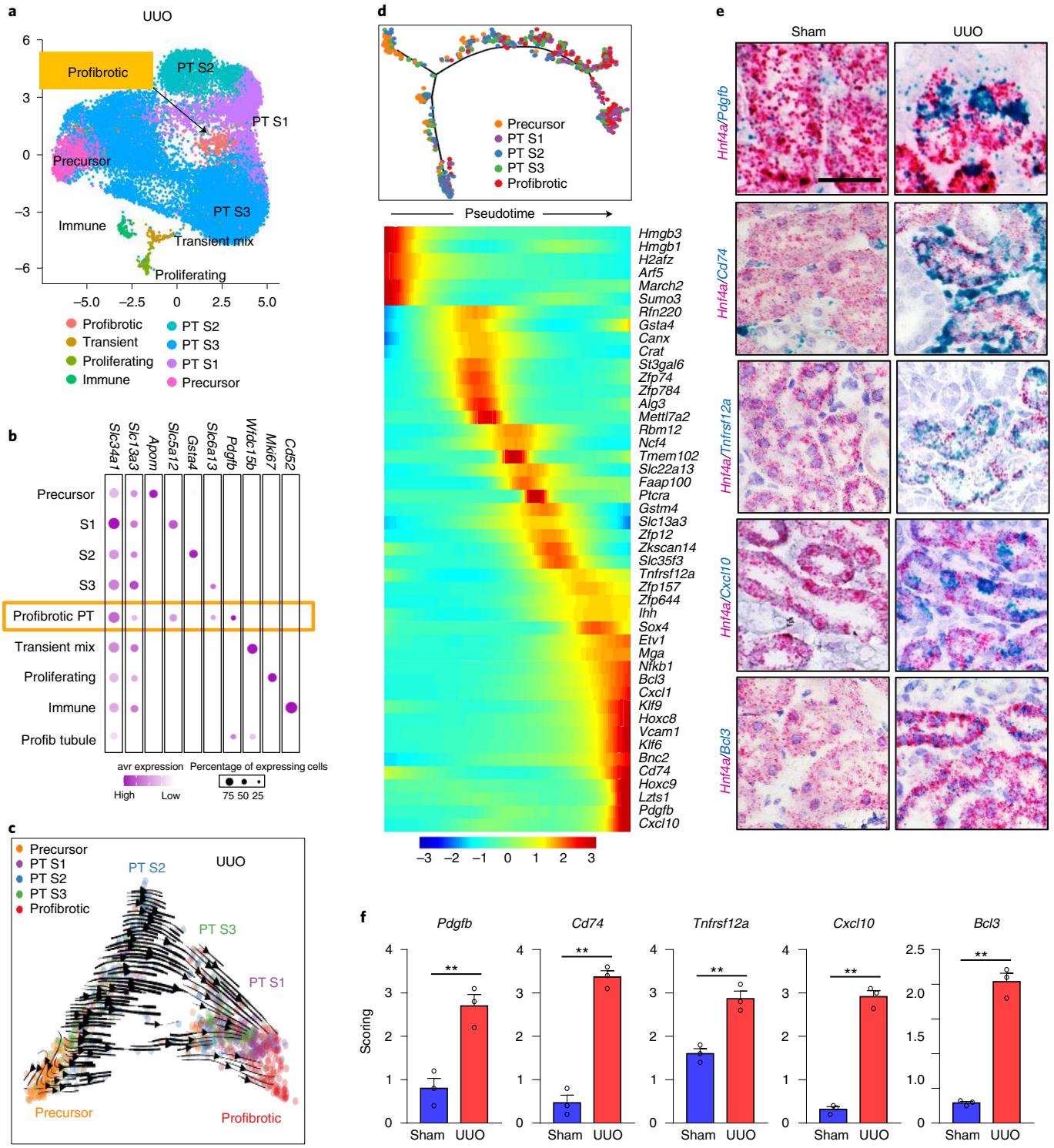

Fig. 2 | Profibrotic proximal tubule cell differentiation in UUO kidneys. a, Subclustering analysis of PT in the UUO kidney. Profibrotic PT cluster is highlighted in orange. **b**, Bubble plot of representative genes in each subcluster *Slc34a1*, *Slc13a3* (PT), *Apom* (precursor PT), *Slc5a12* (S1), *Gsta4* (S2), *Slc6a13* (S3), *Pdgfb* (profibrotic PT), *Wfdc15b* (transient mixed PT), *Mki67* (proliferating PT) and *Cd52* (immune). **c**, RNA velocity cell trajectory analysis of proximal tubule cells in the UUO model of kidney fibrosis. **d**, Genes showing change in expression along the cell differentiation trajectory by Monocle. Red indicates higher expression, blue indicate lower expression. **e**, Representative double in situ hybridization images of *Hnf4a* (PT marker) and gene expressed by profibrotic PT cells, *Pdgfb*, *Cd74*, *Tnfrsf12a*, *Cxcl10* and *Bcl3* in sham and UUO kidneys. Scale bars, 20 μm. Data are representative of three independent experiments. **f**, Semi-quantification of the double in situ hybridization images for *Pdgfb*, *Cd74*, *Tnfrsf12a*, *Cxcl10* and *Bcl3* in sham and UUO kidneys ($n = 3$ in each). $^{**}P < 0.01$. Data are presented as mean ± s.e.m. and were analyzed using a two-tailed Student's *t*-test.

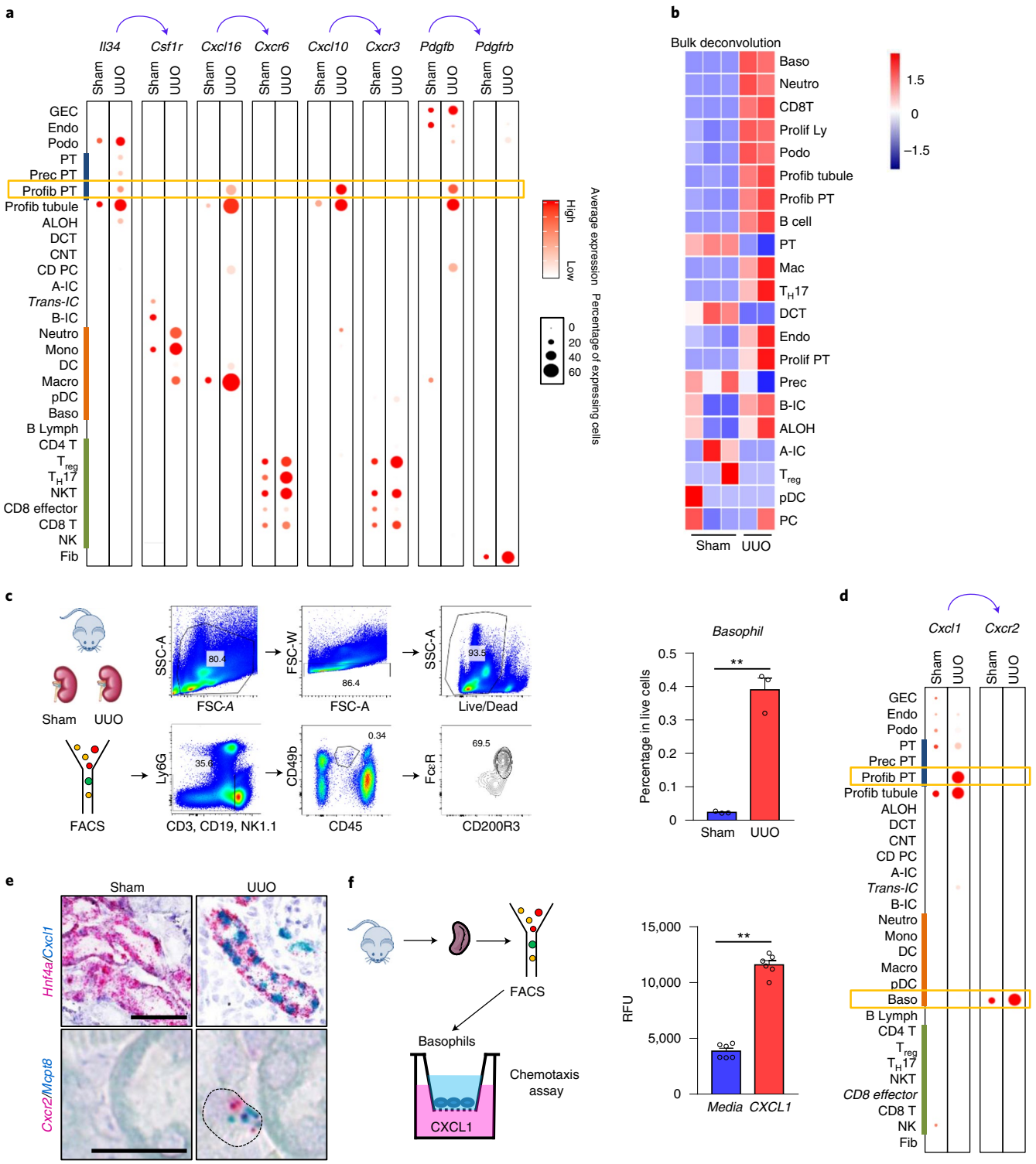

Fig. 3 | The interaction between profibrotic PT cells and basophils in kidney fibrosis. a, Bubble plots showing the average gene expression levels and percentage of expressing cells across all cell types in sham and UUO kidneys. Arrows show the direction of ligand–receptor interaction. The following interaction are shown *Il34–Csf1r*, *Cxcl16–Cxcr6*, *Cxcl10–Cxcr3* and *Pdgfb–Pdgfrb*. **b**, Heat map of the deconvolution analysis of bulk RNA-seq of sham and UUO kidneys. Red indicates higher relative cell fraction, blue indicates lower relative cell fraction. The cell clusters were ranked by the significance (between sham and UUO) from top to bottom. **c**, The flow cytometry strategy of kidney basophil detection and quantification in sham and UUO kidneys from WT mice ($n = 3$ in each). The gating strategy is also shown in Supplementary Fig. 6. $^{**}P < 0.01$. **d**, Bubble plots showing the average gene expression levels and percentage of expressing *Cxcl1-Cxcr2* in sham and UUO kidneys. **e**, Representative double in situ hybridization images of *Hnf4a* (PT marker) with *Cxcl1* (profibrotic PT) and *Mcpt8* (basophil marker) and *Cxcr2* (basophil). Scale bars, 50 μm (top) and 5 μm (bottom). Data are representative of two independent experiments. **f**, Basophil chemotaxis assay. Basophils were isolated from WT mice by FACS and stimulated with culture medium or CXCL1 (10 nM). The migrated basophils were measured by fluorescent dye loading of cells (expressed as RFU, relative fluorescence units) ($n = 6$ in each condition). $^{**}P < 0.01$. Data are presented as mean ± s.e.m. (**c**,**f**) and were analyzed using a two-tailed Student's *t*-test.

In silico cell–cell interaction analysis indicated a predicted interaction between profibrotic PT cells expressing *Cxcl1* and basophils expressing its receptor *Cxcr2* (Fig. 3d). In situ hybridization confirmed the expression of *Cxcl1* in PT cells in UUO kidneys (coexpressed with PT marker *Hnf4a*) and *Cxcr2*, the receptor for *Cxcl1* in basophils (coexpressed with basophil marker *Mcpt8*) (Fig. 3e). Indeed, in vitro chemotaxis assay using flow-sorted basophils showed that CXCL1 treatment alone was sufficient to enhance basophil migration in vitro (Fig. 3f).

In summary, single-cell interaction analysis indicated that secreted cytokines and chemokines by profibrotic PT cells are likely responsible for the recruitment of immune cells in UUO kidneys. An unanticipated interaction of profibrotic PT cells with basophils identified the role of CXCL1 in basophils recruitment.

Depletion of basophils protected from renal fibrosis. To explore the functional role of basophils in renal fibrosis, we crossed the Mcpt8^{Cre} mice with diphtheria toxin receptor (DTR)-expressing mice. MCPT8 is a basophil-specific marker and Mcpt8^{Cre}/DTR mice have been used to study the role of basophils in a variety of conditions[28,29]. We injected Mcpt8^{Cre}/DTR mice with diphtheria toxin (DT), at a dose of 240 ng DT per 20 gr body weight[29] (Fig. 4a). UUO was performed 3 d after the first DT injection and kidneys were collected 7 d after UUO. Flow cytometry analysis confirmed the successful depletion of basophils in kidneys of Mcpt8^{Cre}/DTR mice (Fig. 4b). Expression of *Col1a1*, *Col3a1*, *Timp1* and *Acta2* was higher in UUO kidneys and their levels were observably lower in UUO kidneys of Mcpt8^{Cre}-DTR mice compared to wild-type mice (Fig. 4c). The severity of tubular interstitial damage and renal fibrosis in UUO kidneys were mitigated in Mcpt8^{Cre}/DTR mice (Fig. 4d,e).

To investigate the therapeutic potential of basophil depletion in renal fibrosis, we tested the effect of the MAR-1 antibody. Antibody-mediated basophil depletion (by MAR-1 antibody) has been used in multiple previous studies[7,30]. We injected MAR-1 antibody for three consecutive days into wild-type mice, followed by UUO surgery and kidneys were collected 7 d later (Fig. 4f). Expression of fibrosis markers; *Col1a1*, *Col3a1*, *Timp1* and *Acta2* were higher in UUO kidneys, whereas their levels were lower in MAR-1 antibody-injected wild-type mice when compared to isotype control IgG-injected wild-type mice (Fig. 4g). Histological alterations, such as tubule atrophy and collagen accumulation were also attenuated in UUO kidneys of MAR-1 antibody-injected wild-type mice (Fig. 4h,i). Together, these two complementary approaches to basophil depletion identified the contribution of basophils in the development of renal fibrosis.

Basophils are the source of IL-6 in kidney fibrosis. Next, we set out to explore the mechanism of basophil-mediated kidney fibrosis. Our single-cell analysis indicated higher expression of *Il6*, an important secreted cytokine in basophils of UUO kidneys (Fig. 5a). In addition, the expression of *Il18r1* and *Il1rl1* (receptors for *Il18* and *Il33*, respectively) was also higher in basophils of UUO kidneys (Fig. 5a). Consistently, bulk RNA-seq data showed higher *Il6*, *Il18r1* and *Il1rl1* expression in UUO kidneys compared to shams, but *Il4* expression levels did not show the observable difference (Fig. 5a,b).

To confirm basophil activation and cytokine secretion, we used FACS to isolate basophils and cultured them in the presence of IL-18 or IL-33 (Fig. 5c and Supplementary Fig 7a,b). Following recombinant IL-18 or IL-33 treatment, we observed markedly increased IL-6 levels (measured by ELISA) in the supernatant (Fig. 5c). In situ hybridization further validated high *Il6* expression in basophils (*Mcpt8*-positive cells) in UUO kidneys (Fig. 5d). Consistent with the contribution of basophils as a source of IL-6, we found that the transcript and protein expression levels of IL-6 were observably lower in UUO kidneys following genetic (Mcpt8^{Cre}-DTR) or antibody-mediated (MAR-1) basophil depletion (Fig. 5e,f). *Il18* and *Il33* mRNA and protein expressions were detected mainly in the stroma and their levels were higher in UUO kidneys compared to sham kidneys (Extended Data Fig. 5a–c). Collectively, these data indicate that basophils are a source of IL-6 and basophil activation is provoked in response to IL-18 and IL-33 in UUO kidneys.

IL-6 receptor blockage protected from renal fibrosis. Our studies indicated the role of basophils in IL-6 production in UUO kidneys. To test the role of IL-6 in kidney disease development, we injected wild-type mice with anti-IL-6 receptor (IL-6R) antibody or isotype control IgG every 3 d and induced kidney fibrosis by UUO. Kidneys were collected 7 d after UUO (Fig. 6a). The expression levels of fibrosis markers, including *Col1a1*, *Col3a1*, *Timp1* and *Acta2* and collagen accumulation were lower in UUO kidneys of the anti-IL-6R antibody-treated wild-type mice compared to the isotype control IgG-treated wild-type mice (Fig. 6b,c).

Next, we wanted to understand the mechanism of basophil-mediated fibrosis development. First, we estimated immune cell fractions by quantitative PCR with reverse transcription (qRT–PCR) in UUO kidneys following basophil depletion. We found that levels of *Ccr6*, a top marker gene of T_H17 cells were lower, whereas other immune cell type markers failed to show the observable change in UUO kidneys of mice with genetic depletion of basophils (Mcpt8^{Cre}-DTR) (Extended Data Fig. 6 and Supplementary Table 1). We confirmed the reduction in T_H17 cells in UUO kidneys following genetic basophil depletion by flow cytometric analysis. FACS analysis indicated no observable change in CD4$^+$ T, CD8$^+$ T, T_{reg} and mast cells in kidneys of mice with genetic deletion of basophils (Extended Data Fig. 7a,b).

Multiple previous reports demonstrated the role of IL-6 in regulating T_H17 cell differentiation from CD4$^+$ T cells[31]. Consistently, our single-cell RNA-seq detected higher *Il6ra* and *Il6st*, receptors of *Il6*, in CD4$^+$ T and T_H17 cells in UUO kidneys (Fig. 6d). RNA velocity analysis indicated enhanced differentiation of T_H17 cells from CD4$^+$ T cells in UUO kidneys (Fig. 6e). Monocle trajectory analysis showed consistent CD4$^+$ T cells differentiation toward T_H17 and T_{reg}

Fig. 4 | Mice with genetic or antibody-mediated depletion of basophils are protected from renal fibrosis. a, Experimental design. Mcpt8^{Cre} mice were crossed with DTR mice. Mcpt8^{Cre}-DTR mice were treated with DT (240 ng per 20 g body weight) on D1, D5 and D9. UUO surgery was performed on D4 and mice were killed on D11. **b**, The percentage of basophil detected by FACS in kidney samples of experimental groups ($n=3$). $^{**}P<0.01$. **c**, Relative transcript level of *Col1a1*, *Timp1* and *Acta2* in experimental groups ($n=6$ in each group). Gene expression levels were normalized to *Gapdh*. $^{*}P<0.05$, $^{**}P<0.01$. **d**, The representative images and semi-quantitative analysis of hematoxylin and eosin (H&E) staining in experimental groups ($n=6$ in each group). Scale bars, 20 μm. $^{*}P<0.05$. **e**, The representative images and quantitative analysis of Sirius red staining in experimental groups ($n=6$ in each group). Scale bars, 20 μm. $^{*}P<0.05$. **f**, Experimental design. WT mice were injected intraperitoneally with the MAR-1 antibody or isotype control IgG for three consecutive days (D1, D2 and D3). UUO was performed at D4 and mice were killed on D11. **g**, Relative transcript level of *Col3a1*, *Col1a1*, *Timp1* and *Acta2* in sham and UUO kidneys of WT mice injected with isotype control IgG or MAR-1 antibody ($n=6$ in each group). Gene expression levels were normalized to *Gapdh*. $^{*}P<0.05$, $^{**}P<0.01$. **h**, The representative images and semi-quantitative analysis of H&E staining in experimental groups ($n=6$ in each group). Scale bars, 20 μm. $^{*}P<0.05$. **i**, Representative images and quantitative analysis of Sirius red staining in experimental groups ($n=6$ in each group). Scale bars, 20 μm. $^{*}P<0.05$. Data are presented as mean ± s.e.m. (**b**–**e**,**g**–**i**) and were analyzed using a one-way analysis of variance (ANOVA) followed by Tukey post hoc test for multigroup comparison.

cells (Fig. 6f). T_H17 cells were enriched for *Il17a* and *Tgfb1* (Fig. 6f). The expression levels of *Il17a* and *Tgfb1* were higher in UUO kidneys, but their levels were lower in UUO kidneys of mice with basophil depletion (Fig. 6g).

In summary, these results demonstrated the contribution of IL-6 and T_H17 as downstream mediators in kidney fibrosis.

Higher *IL6* and basophil numbers in human kidney fibrosis. Our animal model studies identified a role for basophils in the development of renal fibrosis. To determine relevance of these findings to human kidney fibrosis, a feature of CKD, we performed single-cell RNA-seq of human kidneys from healthy control and CKD samples. Following quality control and filtering low-quality cells, we identified 13,380 cells and 17 cell clusters. We were able to annotate basophil/mast cell clusters in human kidney samples and this cluster mainly (94% of cells) originated from the fibrotic kidney (Fig. 7a, Supplementary Fig 8 and Supplementary Table 5). We could not separate basophils and mast cells due to their similarities in the overall cell clustering, however, the subclustering analysis indicated the heterogeneous expression of *KIT*, a marker of mast

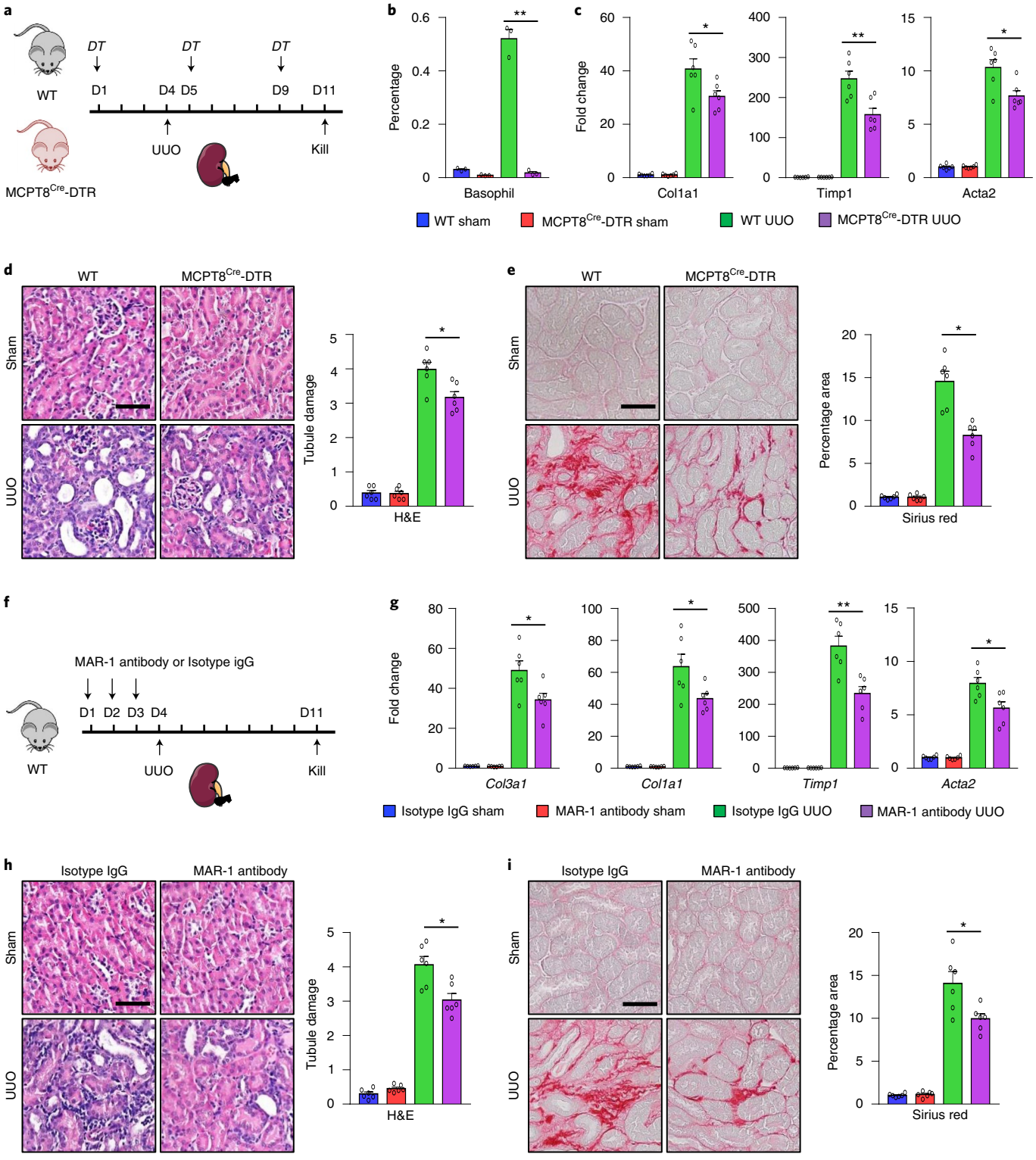

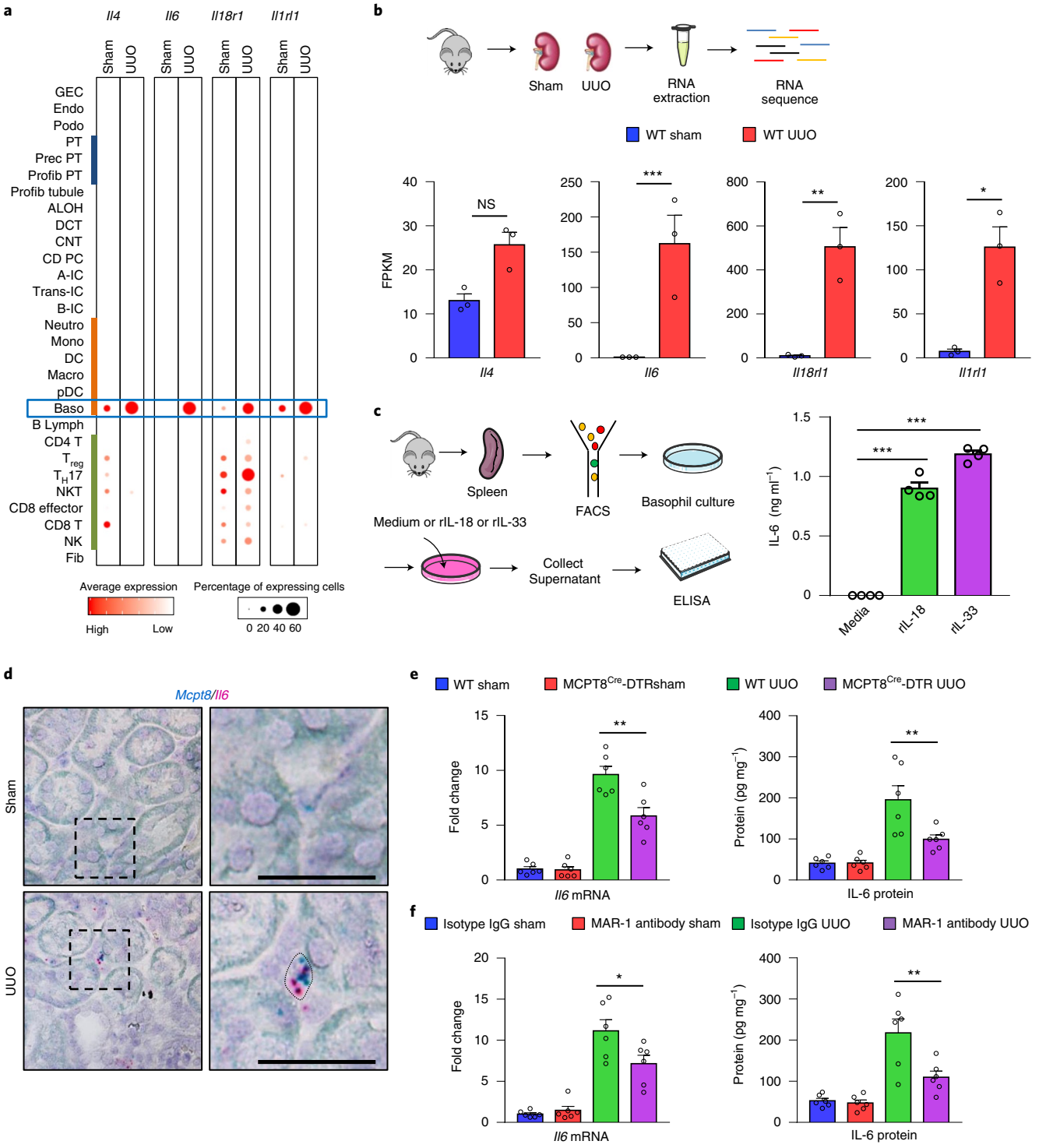

Fig. 5 | Basophil respond to IL-18 and IL-33 and release IL-6 in UUO kidneys. a, Bubble plots showing the average gene expression and percentage of expressing cells *Il4*, *Il6*, *Il18r1* and *Il1rl1* in sham and UUO kidneys. **b**, The relative expression (FPKM) levels of *Il4*, *Il6*, *Il18r1* and *Il1rl1* in sham and UUO kidneys of WT mice by bulk RNA-seq ($n = 3$, respectively). $^{*}P < 0.05$, $^{**}P < 0.01$, $^{***}P < 0.001$; NS, not significant. Significance was determined using DESeq2. **c**, In vitro basophil stimulation assay. Basophils were cultured and stimulated with medium only, or recombinant IL-18 and IL-33 (rIL-18 and rIL-33) in the absence of IL-3. IL-6 levels were measured in the supernatant ($n = 4$ in each condition). $^{***}P < 0.001$. **d**, Representative double in situ hybridization images of *Il6* with *Mcpt8* (basophil) in sham and UUO kidneys of WT mice. Enlarged image of the box in the left image (right). Scale bars, 20 μm. Data are representative of two independent experiments. **e**, The mRNA and protein expression levels of IL-6 in sham and UUO kidneys of WT mice and mice with genetic depletion of basophils (Mcpt8^{Cre}-DTR) ($n = 6$ in each group). Gene expression levels were normalized to *Gapdh*. IL-6 protein levels were normalized for total protein amount. $^{**}P < 0.01$. **f**, The mRNA and protein expression levels of IL-6 in sham and UUO kidneys of WT mice with isotype control IgG or MAR-1 antibody injection ($n = 6$ in each group). Gene expression levels were normalized to *Gapdh*. IL-6 protein levels were normalized for total protein levels. $^{*}P < 0.05$, $^{**}P < 0.01$. Data are presented as mean values ± s.e.m. (**b**,**c**,**e**,**f**) and were analyzed using a one-way ANOVA followed by Tukey post hoc test for multigroup comparison.

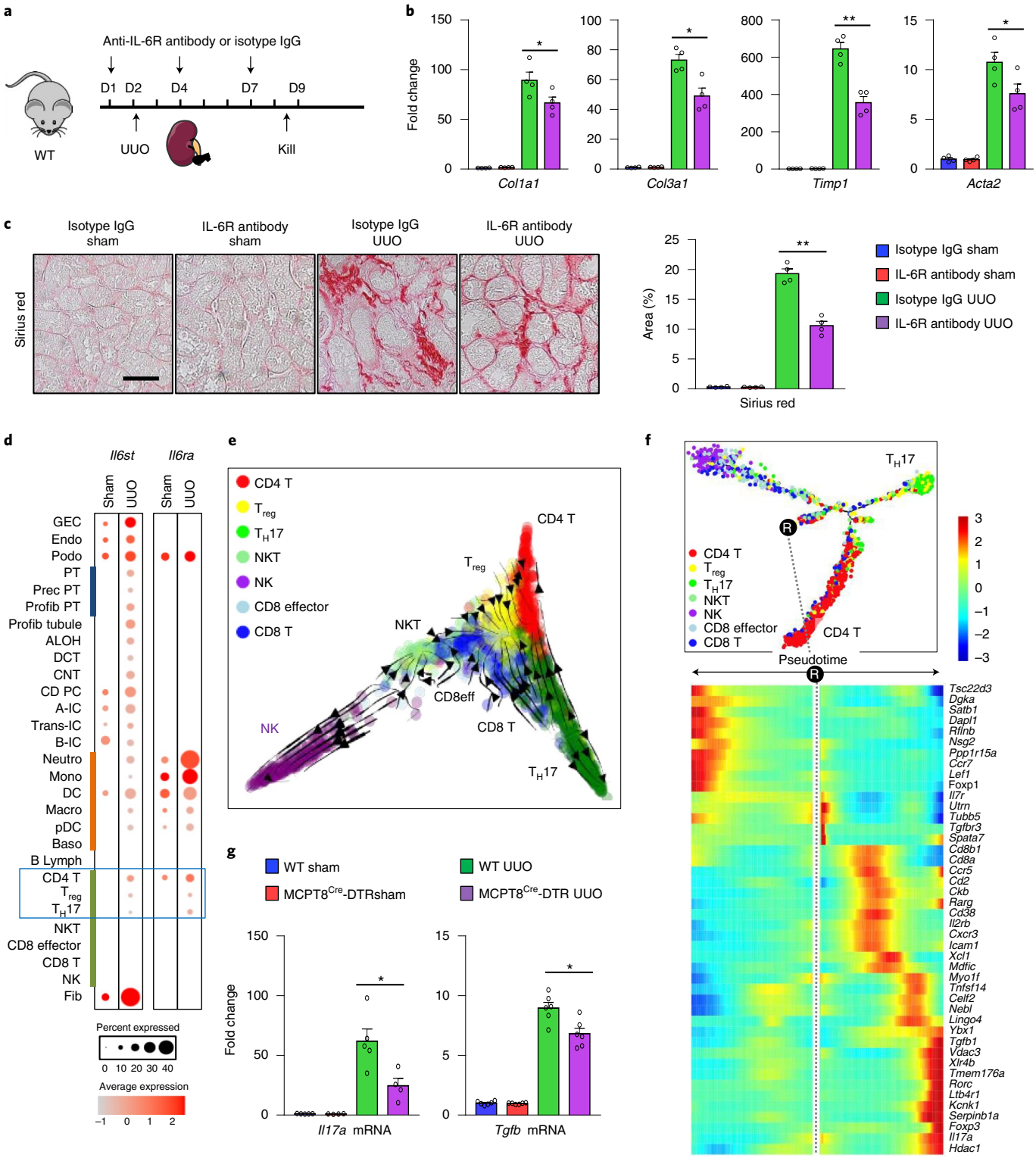

Fig. 6 | IL-6 receptor blockade protected from renal fibrosis and T_H17 cell expansion. a, Experimental design. The anti-IL-6R Ab (400 μg) or isotype control IgG were injected into WT mice intraperitoneally at D1, D4 and D7. UUO was performed at D2 and mice were killed at D9. **b**, Relative transcript level of *Col1a1*, *Col3a1*, *Timp1* and *Acta2* in sham and UUO kidneys of experimental groups ($n = 4$ in each group). Gene expression levels were normalized to *Gapdh*. $^*P < 0.05$, $^{**}P < 0.01$. **c**, The representative images and quantitative analysis of Sirius red staining in experimental groups ($n = 4$ in each group). Scale bars, 20 μm. $^{**}P < 0.01$. **d**, Bubble plots showing the average gene expression and percentage of expressing cells of *Il6st* and *Il6ra* in sham and UUO kidneys. **e**, RNA velocity analysis of T lymphocytes in UUO kidneys, showing $CD4^+$, $CD8^+$, $CD8^+$ effector, T_H17, T_{reg} cells, NK and NKT cells. **f**, Cell trajectory analysis by Monocle and heat map showing changes in expression of genes along the differentiation trajectory. **g**, Relative transcript level of *Il17a* and *Tgfb1* in sham and UUO kidneys of WT mice and mice with genetic depletion of basophils ($Mcpt8^{Cre}$-DTR) ($n = 6$ in each group). Gene expression levels were normalized to *Gapdh*. $^*P < 0.05$. Data are presented as mean ± s.e.m. (**b**,**c**,**g**) and were analyzed using a one-way ANOVA followed by Tukey post hoc test for multigroup comparison.

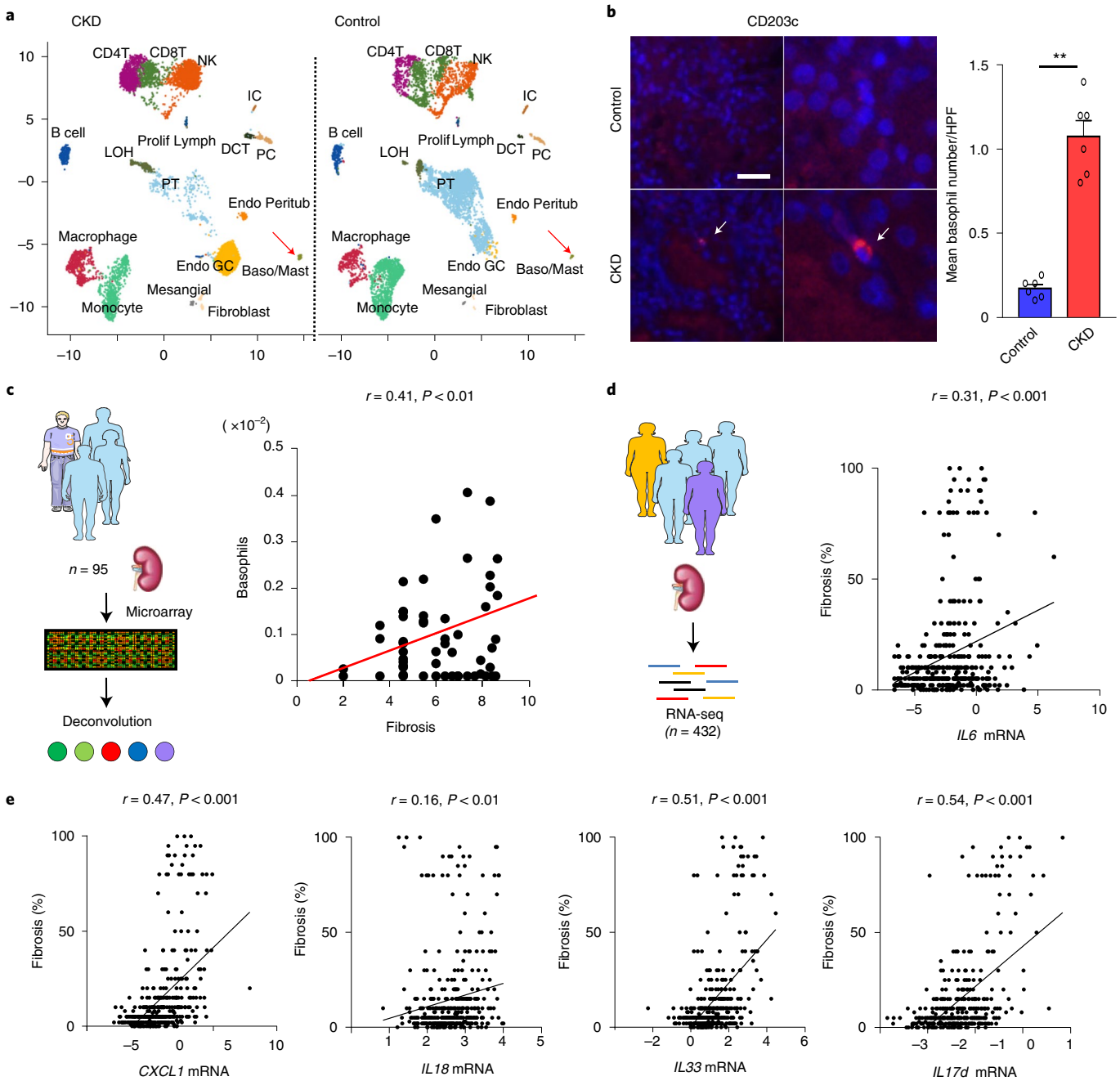

Fig. 7 | Increased number of basophils in kidneys of patients with CKD. a, Single-cell analysis of healthy control and CKD human kidney samples. Basophil/mast cell cluster was highlighted with red arrow. Note that the increase in number of basophils/mast cells in CKD samples. **b**, Representative immunofluorescence staining of CD203c (activated basophils) and quantification of basophil numbers in healthy control and CKD kidneys ($n = 6$, respectively). Higher magnification image of image on left (right). Arrow points to basophils. Scale bars, 20 μm. $^{**}P < 0.01$. Data are presented as mean ± s.e.m. Data were analyzed using a two-tailed Student's *t*-test. **c**, In silico deconvolution analysis of bulk microarray data 95 human kidney samples with variable degree of fibrosis. The correlation plot of basophils fraction (determined by in silico deconvolution) (*y* axis) and the percentage (log expression) of renal fibrosis (*x* axis) is shown. **d**, RNA-seq data from 432 human kidney tubule samples. Correlation between the percentage of renal fibrosis (*y* axis) and normalized *IL6* levels (*x* axis). **e**, Correlation between the percentage of renal fibrosis (*y* axis) and normalized expression levels of *CXCL1*, *IL18*, *IL33* and *IL17d* (*x* axis) in human kidney samples. The *r* represents Pearson's correlation coefficient values (**c**–**e**).

cell and *CD63*, a marker of basophils, allowing us to differentiate these two cell types (Supplementary Fig. 9). Next, we stained basophils with CD203c (2D7), a marker of activated human basophils, in healthy control or CKD human kidney samples. Basophils were exceedingly rare in healthy control human kidneys, but their number was higher in CKD kidneys (Fig. 7b). Furthermore, deconvolution of bulk RNA-seq analysis of microarray samples obtained from kidneys of 95 patients with and without diabetes and hypertension with variable degree of fibrosis showed a clear correlation between basophil number and renal fibrosis (Fig. 7c and Supplementary Table 6). In addition, the degree of kidney fibrosis positively correlated with the number of $CD4^+$ T, $CD8^+$ effector T, T_H17, T_{reg}, NKT, DC, neutrophil or fibroblasts and negatively correlated with the percent of PT cells (Supplementary Fig 10).

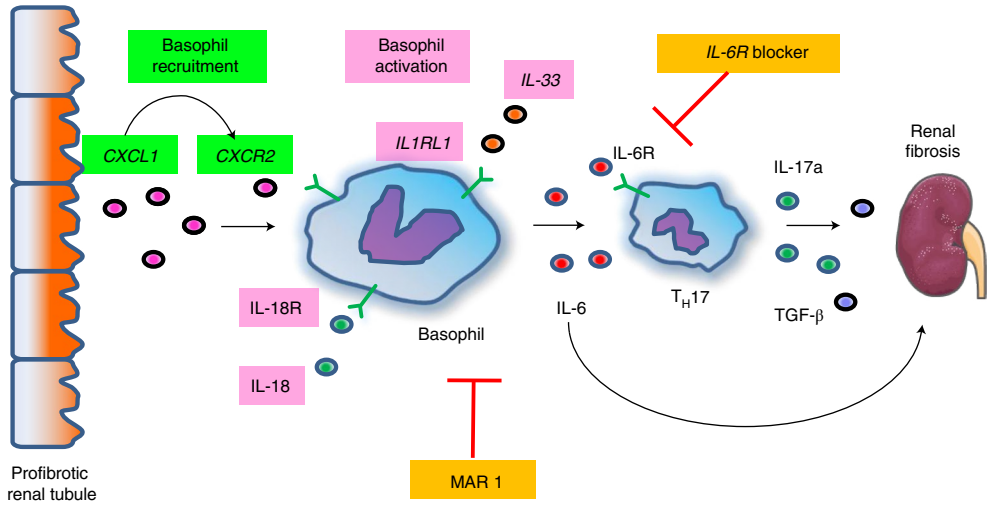

Fig. 8 | Graphical abstract. Injured profibrotic renal tubules release CXCL1, resulting in recruitment of CXCR2-positive basophils to the kidneys. The recruited basophils express IL-18R and IL1RL1 and are activated by their ligands; IL-18 and IL-33. Activated basophils produce IL-6 and promote T_H17 cell expansion. IL-17a and transforming growth factor (TGF)-β released from T_H17 contribute to the development of renal fibrosis. Antibody-mediated basophil depletion (MAR-1) and IL-6 receptor blockade protect from renal fibrosis.

Finally, we looked into transcriptomics data obtained by RNA-seq of 432 microdissected human kidney samples (Supplementary Table 7). The analysis showed a positive correlation between *IL6* expression levels and the severity of fibrosis and a negative correlation between *IL6* expression levels and kidney function (estimated glomerular filtration rate; eGFR) (Fig. 7d and Extended Data Fig. 8a). In addition, *CXCL1*, *IL18*, *IL33* and *IL17d* transcript levels positively correlated with the severity of fibrosis and *IL6* levels, whereas they negatively correlated with eGFR (Fig. 7e and Extended Data Fig. 8a,b). In summary, human kidney analysis highlighted consistent correlations between renal fibrosis and basophil numbers. Furthermore, renal *IL6*, *IL18* and *IL33* expression correlated with CKD severity.

Discussion

While fibrosis is often viewed as unresolved inflammation[32–34], systematic characterization of immune cells in renal fibrosis has not been performed. Here, our single-cell studies identified increased diversity of immune cells and an unappreciated role of basophils in renal fibrosis (Fig. 8). Growing evidence points to the contribution of proximal tubule cells in kidney disease and fibrosis development[35]. Genetic studies indicated enrichment of genes causing kidney dysfunction in PT cells[36]. Single-cell sequencing highlighted the plasticity of PT cells in kidney fibrosis. The overlap of the DEGs between the profibrotic PT cells observed in UUO kidneys and ischemic reperfusion injury and previous publications indicated a common mechanism of kidney injury[22,37]. 'Profibrotic PT' cells, interacted with resident fibroblasts via IHH and PDGFB and myeloid cells via IL-34 and lymphoid cells via CXCL16. The critical role of IL-34 and CXCL16 in renal fibrosis was established by previous studies[27,38]. Here we showed that profibrotic PT cells expressing CXCL1 were likely responsible for basophil recruitment although the roles of other pathways remain to be defined. A previous paper indicated the role of CXCL1 in recruiting granulocytes, including basophils[39]. CXCL1 expression was also enriched in tubule cells weakly expressing proximal tubule marker HNF4A and expressing markers of the descending loop of Henle, indicating the possibility that a similar altered cell population is extending to the bordering segment of PTs.

Our single-cell studies highlighted the increased number of basophils in kidney fibrosis. Basophils show a strong resemblance to mast cells. Here we used a variety of methods to distinguish mast cells from basophils. Our single-cell studies indicated the expression of basophil marker, Mcpt8 and failed to show the mast cell marker, Mcpt4 (ref. [7]). We further confirmed the Mcpt8 expression both by in situ hybridization and by genetic linage tagging. We validated our single-cell expression and in situ studies with gold standard flow cytometry using classic basophil markers such as CD49b, CD200R3 and FceR1. Overall, our comprehensive profiling studies indicated that the analyzed cells are basophils and not mast cells.

We used two complementary methods to define the role of basophils in renal fibrosis, first by genetic depletion using the $Mcpt8^{Cre}$-DTR mice and second by antibody-mediated depletion using the MAR-1 antibody. Mice with genetic deletion or antibody-mediated depletion were protected from renal fibrosis development. We proposed that increased stromal expression of IL-18 and IL-33 likely play role in activating basophils and stimulating IL-6 secretion. Previous studies showed that blocking IL-18 and IL-33 ameliorated renal fibrosis[40,41]. IL-6 has a pleiotropic effect on inflammation and immune response, it could have context-dependent pro- or anti-inflammatory properties[42]. In our animal studies, IL-6R antibody-treated mice were partially protected from renal fibrosis. Previous studies also indicated the profibrotic role of IL-6 in cardiac[43], lung[44] and peritoneal[45] fibrosis, indicating that IL-6 might be a common mediator of fibrosis. Previous studies, however, failed to identify the source of IL-6 in fibrosis. Here we clarified that basophils were a major source of IL-6 in renal fibrosis. This was consistent with a recent paper showing that basophils as the main source of IL-6 in lung development[7].

Basophils have been shown to interact with T_H17 cells and macrophages[7,46]. We found that T_H17 cell number and *IL17a* expression were increased in UUO but they were lower in UUO kidneys of mice with basophil depletion. We confirmed the change in T_H17 cells by FACS and by cell type-specific gene expression profiling. It is noteworthy that our single-cell analysis independently showed a shift toward T_H17 cells in fibrosis. We failed to observe a quantitative change in macrophages; however, we cannot exclude functional differences. T_H17 cells responding to IL-6 are likely to be the downstream mediator of basophils in kidney fibrosis. Our group previously illustrated the contribution of T_H17 cells to renal fibrosis[47] and their role in lung fibrosis has also been established. T_H17 cells can interact with fibroblasts to orchestrate fibro-inflammation[48,49].

Finally, we validated our observations in human kidney samples from patients with fibrosis. We were able to identify a basophil/mast cell cluster in human kidney single-cell sequencing data and we used *KIT* and *CD63* to distinguish basophils and mast cells[50]. We performed immunostaining and in silico deconvolution studies to confirm the increase in basophil number in fibrotic kidneys. Finally, we also showed the increase in expression of *CXCL1*, a chemokine, in patients with kidney fibrosis. The severity of kidney fibrosis correlated with the expression levels of *IL6*, *IL18* and *IL33*, indicating consistent changes between mouse models and patient samples.

Our results have several potential therapeutic implications. First, blocking the IL-6 pathway in renal fibrosis could be utilized. Tocilizumab, a monoclonal antibody to the IL-6 receptor, is approved to use for autoimmune diseases such as rheumatoid arthritis and is currently studied in systemic sclerosis and COVID19-related lung disease[51,52]. Second, antibody or cellular therapy-based depletion of basophils could also be considered.

In conclusion, here we demonstrated that the unique differentiation of proximal tubule cells (profibrotic PT) in kidney fibrosis and their interplay with basophils mediated by CXCL1, the chemokine likely responsible for basophil recruitment. Basophils secreted a large amount of IL-6 in response to IL-18 and IL-33 and interacted with T_H17 cells, orchestrating kidney fibrosis development. Human kidney single-cell and bulk expression studies validated findings of mouse experimental studies. The unexpected and important contribution of basophils to renal fibrosis opens new potential therapeutic avenues for the management of CKD.

Online content

Any methods, additional references, Nature Research reporting summaries, source data, extended data, supplementary information, acknowledgements, peer review information; details of author contributions and competing interests; and statements of data and code availability are available at https://doi.org/10.1038/s41590-022-01200-7.

Received: 15 September 2021; Accepted: 1 April 2022;
Published online: 12 May 2022

References

1. Wynn, T. A. Cellular and molecular mechanisms of fibrosis. *J. Pathol.* **214**, 199–210 (2008).
2. Jager, K. J. et al. A single number for advocacy and communication-worldwide more than 850 million individuals have kidney diseases. *Nephrol. Dialysis Transplant.* **34**, 1803–1805 (2019).
3. Dhillon, P. et al. The nuclear receptor ESRRA protects from kidney disease by coupling metabolism and differentiation. *Cell Metab.* **33**, 379–394 (2021).
4. Galli, S. J., Tsai, M. & Piliponsky, A. M. The development of allergic inflammation. *Nature* **454**, 445–454 (2008).
5. Voehringer, D. Protective and pathological roles of mast cells and basophils. *Nat. Rev. Immunol.* **13**, 362–375 (2013).
6. Inclan-Rico, J. M. et al. Basophils prime group 2 innate lymphoid cells for neuropeptide-mediated inhibition. *Nat. Immunol.* **21**, 1181–1193 (2020).
7. Cohen, M. et al. Lung single-cell signaling interaction map reveals basophil role in macrophage imprinting. *Cell* **175**, 1031–1044 (2018).
8. Bosch, X., Lozano, F., Cervera, R., Ramos-Casals, M. & Min, B. Basophils, IgE, and autoantibody-mediated kidney disease. *J. Immunol.* **186**, 6083–6090 (2011).
9. Schiechl, G. et al. Basophils trigger fibroblast activation in cardiac allograft fibrosis development. *Am. J. Transplant.* **16**, 2574–2588 (2016).
10. Sicklinger, F. et al. Basophils balance healing after myocardial infarction via IL-4/IL-13. *J. Clin. Invest*. https://doi.org/10.1172/JCI136778 (2021).
11. Franco, C. B., Chen, C. C., Drukker, M., Weissman, I. L. & Galli, S. J. Distinguishing mast cell and granulocyte differentiation at the single-cell level. *Cell Stem Cell* **6**, 361–368 (2010).
12. Madjene, L. C. et al. Mast cells in renal inflammation and fibrosis: lessons learnt from animal studies. *Mol. Immunol.* **63**, 86–93 (2015).
13. Higashi, A. Y., Aronow, B. J. & Dressler, G. R. Expression Profiling of fibroblasts in chronic and acute disease models reveals novel pathways in kidney fibrosis. *J. Am. Soc. Nephrol.* **30**, 80–94 (2019).
14. Hewitt, K. J. et al. PDGFRβ expression and function in fibroblasts derived from pluripotent cells is linked to DNA demethylation. *J. Cell Sci.* **125**, 2276–2287 (2012).
15. Heng, T. S. & Painter, M. W. The Immunological Genome Project: networks of gene expression in immune cells. *Nat. Immunol.* **9**, 1091–1094 (2008).
16. Park, J. et al. Single-cell transcriptomics of the mouse kidney reveals potential cellular targets of kidney disease. *Science* **360**, 758–763 (2018).
17. Conway, B. R. et al. Kidney single-cell atlas reveals myeloid heterogeneity in progression and regression of kidney disease. *J. Am. Soc. Nephrol.* **31**, 2833–2854 (2020).
18. Klinkhammer, B. M., Floege, J. & Boor, P. PDGF in organ fibrosis. *Mol. Asp. Med.* **62**, 44–62 (2018).
19. Kusaba, T., Lalli, M., Kramann, R., Kobayashi, A. & Humphreys, B. D. Differentiated kidney epithelial cells repair injured proximal tubule. *PNAS* **111**, 1527–1532 (2014).
20. Nielsen, R., Christensen, E. I. & Birn, H. Megalin and cubilin in proximal tubule protein reabsorption: from experimental models to human disease. *Kidney Int.* **89**, 58–67 (2016).
21. Chen, L., Chou, C. L. & Knepper, M. A. Targeted single-cell RNA-seq identifies minority cell types of kidney distal nephron. *J. Am. Soc. Nephrol.* **32**, 886–896 (2021).
22. Gerhardt, L. M. S., Liu, J., Koppitch, K., Cippà, P. E. & McMahon, A. P. Single-nuclear transcriptomics reveals diversity of proximal tubule cell states in a dynamic response to acute kidney injury. *PNAS* https://doi.org/10.1073/pnas.2026684118 (2021).
23. Muto, Y. et al. Single cell transcriptional and chromatin accessibility profiling redefine cellular heterogeneity in the adult human kidney. *Nat. Commun.* **12**, 2190 (2021).
24. Liu, S. S. et al. Targeting degradation of the transcription factor C/EBPβ reduces lung fibrosis by restoring activity of the ubiquitin-editing enzyme A20 in macrophages. *Immunity* **51**, 522–534 (2019).
25. Petrovic-Djergovic, D. et al. CXCL10 induces the recruitment of monocyte-derived macrophages into kidney, which aggravate puromycin aminonucleoside nephrosis. *Clin. Exp. Immunol.* **180**, 305–315 (2015).
26. Ruth, J. H. et al. CXCL16-mediated cell recruitment to rheumatoid arthritis synovial tissue and murine lymph nodes is dependent upon the MAPK pathway. *Arthritis Rheum.* **54**, 765–778 (2006).
27. Baek, J. H. et al. IL-34 mediates acute kidney injury and worsens subsequent chronic kidney disease. *J. Clin. Invest.* **125**, 3198–3214 (2015).
28. Sullivan, B. M. et al. Genetic analysis of basophil function in vivo. *Nat. Immunol.* **12**, 527–535 (2011).
29. El Hachem, C. et al. Treatment of MCPT8(DTR) mice with high- or low-dose diphtheria toxin leads to differential depletion of basophils and granulocyte-macrophage progenitors. *Eur. J. Immunol.* **48**, 861–873 (2018).
30. Denzel, A. et al. Basophils enhance immunological memory responses. *Nat. Immunol.* **9**, 733–742 (2008).
31. Yuk, C. M. et al. Basophil-derived IL-6 regulates T(H)17 cell differentiation and CD4 T cell immunity. *Sci. Rep.* **7**, 41744 (2017).
32. Tang, P. M., Nikolic-Paterson, D. J. & Lan, H. Y. Macrophages: versatile players in renal inflammation and fibrosis. *Nat. Rev. Nephrol.* **15**, 144–158 (2019).
33. Turner, J. E., Becker, M., Mittrücker, H. W. & Panzer, U. Tissue-resident lymphocytes in the kidney. *J. Am. Soc. Nephrol.* **29**, 389–399 (2018).
34. Kurts, C., Ginhoux, F. & Panzer, U. Kidney dendritic cells: fundamental biology and functional roles in health and disease. *Nat. Rev. Nephrol.* **16**, 391–407 (2020).
35. Gewin, L. S. Renal fibrosis: primacy of the proximal tubule. *Matrix Biol.* **68–69**, 248–262 (2018).
36. Qiu, C. et al. Renal compartment-specific genetic variation analyses identify new pathways in chronic kidney disease. *Nat. Med.* **24**, 1721–1731 (2018).
37. Kirita, Y., Wu, H., Uchimura, K., Wilson, P. C. & Humphreys, B. D. Cell profiling of mouse acute kidney injury reveals conserved cellular responses to injury. *PNAS* **117**, 15874–15883 (2020).
38. Liang, H. et al. CXCL16 deficiency attenuates renal injury and fibrosis in salt-sensitive hypertension. *Sci. Rep.* **6**, 28715 (2016).
39. Geiser, T., Dewald, B., Ehrengruber, M. U., Clark-Lewis, I. & Baggiolini, M. The interleukin-8-related chemotactic cytokines GRO α, GRO β, and GRO γ activate human neutrophil and basophil leukocytes. *J. Biol. Chem.* **268**, 15419–15424 (1993).
40. Bani-Hani, A. H. et al. IL-18 neutralization ameliorates obstruction-induced epithelial-mesenchymal transition and renal fibrosis. *Kidney Int.* **76**, 500–511 (2009).
41. Liang, H. et al. Interleukin-33 signaling contributes to renal fibrosis following ischemia reperfusion. *Eur. J. Pharmacol.* **812**, 18–27 (2017).
42. Hunter, C. A. & Jones, S. A. IL-6 as a keystone cytokine in health and disease. *Nat. Immunol.* **16**, 448–457 (2015).
43. González, G. E. et al. Deletion of interleukin-6 prevents cardiac inflammation, fibrosis and dysfunction without affecting blood pressure in angiotensin II-high salt-induced hypertension. *J. Hypertens.* **33**, 144–152 (2015).

44. Le, T. T. et al. Blockade of IL-6 trans signaling attenuates pulmonary fibrosis. *J. Immunol.* **193**, 3755–3768 (2014).
45. Fielding, C. A. et al. Interleukin-6 signaling drives fibrosis in unresolved inflammation. *Immunity* **40**, 40–50 (2014).
46. Wakahara, K. et al. Human basophils interact with memory T cells to augment Th17 responses. *Blood* **120**, 4761–4771 (2012).
47. Coppock, G. M. et al. Loss of IL-27Rα results in enhanced tubulointerstitial fibrosis associated with elevated Th17 responses. *J. Immunol.* **205**, 377–386 (2020).
48. Wilson, M. S. et al. Bleomycin and IL-1β-mediated pulmonary fibrosis is IL-17A dependent. *J. Exp. Med.* **207**, 535–552 (2010).
49. Cipolla, E. et al. IL-17A deficiency mitigates bleomycin-induced complement activation during lung fibrosis. *FASEB J.* **31**, 5543–5556 (2017).
50. Mitsui, H. et al. Development of human mast cells from umbilical cord blood cells by recombinant human and murine c-kit ligand. *PNAS* **90**, 735–739 (1993).
51. Khanna, D. et al. Tocilizumab in systemic sclerosis: a randomised, double-blind, placebo-controlled, phase 3 trial. *Lancet Resp. Med.* **8**, 963–974 (2020).
52. Guaraldi, G. et al. Tocilizumab in patients with severe COVID-19: a retrospective cohort study. *Lancet Rheumatol.* **2**, e474–e484 (2020).

Methods

Mice. Animal studies were approved by the Institutional Animal Care and Use Committee of the University of Pennsylvania. Mcpt8^{Cre} mice were provided by A. M. Piliponsky (Seattle Children's Research Institute). DTR mice were purchased from the Jackson laboratory (009669). Mcpt8^{Cre}-DTR mice were injected with DT every 4 d at 240 ng per 20 g body weight intraperitoneally. The left ureter was ligated with 4-0 silk to induce UUO injury. UUO was performed 3 d after the first DT injection. For antibody-mediated depletion of basophils, WT mice were injected intraperitoneally twice daily with 5 µg of Armenian anti-mouse FcεRIα antibody (16-5898-85, clone; MAR-1, eBioscience) for 3 d or isotype control IgG antibody (16-4888-85, Armenian hamster IgG, eBioscience). UUO was performed 1 d after last the MAR-1 antibody injection. For IL-6 receptor blockade, 400 µg anti-IL-6R (BE0047, clone 15A7; BioXCell) or isotype control IgG (BE0090, BioXCell) was injected every 3 d. UUO was performed 1 d after first the anti-IL-6R injection. In all experiments, mice were killed at 7 d after UUO surgery. All mice were C57BL/6 background and male mice were used at age 8–12 weeks in all experiments. Mice were housed under specific-pathogen-free conditions with a 12-h dark/light cycle, at 22–25 °C and 50–60% humidity with water and food provided ad libitum. No statistical methods were used to predetermine sample size, but our sample sizes are similar to those reported in previous publications[53]. Age-matched mice were randomly assigned to experimental conditions. Our research complies with the ethical regulations stipulated by the University of Pennsylvania.

Preparation of single-cell suspension. Mice were perfused with chilled 1× PBS via the left heart. Samples were minced into 1-mm^3 cubes and digested using the Multi Tissue dissociation kit (Miltenyi, 130-110-201). The tissue was homogenized using 21 G and 26 1/2 G syringes. Up to 0.25 g of the tissue was digested with 50 µl of Enzyme D, 25 µl of Enzyme R and 6.75 µl of Enzyme A in 1 ml of RPMI and incubated for 30 min at 37 °C. The reaction was deactivated by 10% fetal bovine serum (FBS). The solution was then passed through a 40-µm cell strainer. After centrifugation at 800*g* for 5 min, the cell pellet was incubated with 1 ml of RBC lysis buffer on ice for 3 min. Cell number and viability were analyzed using Countess AutoCounter (Invitrogen, C10227). This method generated single-cell suspension with greater than 80% viability.

Two fresh human samples were collected from the patients who were under nephrectomy. The tissues were checked by the pathologist to be free of tumor. The procedure was approved by the Institutional Review Board of the University of Pennsylvania. Nephrectomies were de-identified and as the corresponding clinical information was collected by an honest broker; the subjects were exempted from the consent. The single-cell suspension protocol was similar to mouse single-cell suspension preparation except for the longer incubation time (35 min). Briefly, the single-cell suspension was loaded onto a well on a 10X Chromium Single-Cell instrument (v.5.00, b01) (10X Genomics). The cDNA libraries were constructed using the 10X Chromium Single cell 3′ Library kit (CG000183) according to the manufacturer's protocol. Libraries were sequenced on an Illumina HiSeq 2000 or NextSeq 550 2×150 paired-end kits.

Alignment and generation of data matrix. The mouse and human kidney single cell data were aligned using CellRanger v.6.0.1 (10X Genomics) using mouse (GRCm38) and human genome reference Ensembl 93 (GRCh38). The filtered matrix output of CellRanger was used to make Seurat object for each sample with genes expressed in more than three cells and cells with at least 300 genes by using Seurat (v.4.0.3)[54]. The Seurat objects were merged and used for downstream analysis.

Quality control and unbiased clustering of single-cell RNA-seq. The low-quality cells were filtered: such as cells with mitochondrial counts >50 % and n_Feature_RNA < 200 or n_Feature_RNA > 3,000 t. The top variable genes were identified using the 'vst' method. Next, the data was normalized and scaled in terms of n_Count_RNA and mitochondrial percentage genes. The scaled data were used for principal component analysis using 30 principal components. To remove batch effect, Harmony (v.1.0)[55] was used. To cluster cells, the results of harmony were projected to UMAP, then a shared nearest-neighbor network was created based on Euclidian distances between cells in 30 principal component spaces. To identify DEGs in each cell types, the 'FindAllMarkers' function of the Seurat with the following parameters was used: logfc.threshold, 0.25 and adjusted *P* value <0.05. The 'MAST' test was used for DEG analysis.

Removal of doublet-like cells. Doublet-like cells were identified using DoubletFinder (v.2.0.3)[56] which is a computational doublet detection tool. The number of expected doublets was calculated for each sample based on the expected rates of doublets which are provided by 10X Genomics.

Integration of present dataset with publicly available data. To understand similarities and differences with the publicly available UUO dataset (GSE140023), we performed an integrated analysis. Both datasets (present and published) were realigned using CellRanger 6.0.1 and then, the filtered matrix output was used to make Seurat object for each sample with genes expressed in more than three cells and cells with at least 300 genes by using Seurat (v.4.0.3) were created and then merged. Filtering, data normalization and unbiased clustering were performed on the merged dataset as described above. Harmony was used for batch correction and integration.

Cell trajectory analysis and RNA velocity. To construct single-cell pseudotime trajectory and to identify genes that change as the cells undergo transition, the Monocle2 (v.2.4.0) algorithm was applied to proximal tubule and immune cells[57]. First, equal number of cells per cluster were randomly selected from each cell clusters. Genes were selected if they were expressed in ≥10 cells, their mean expression value was ≥0.1 and the dispersion empirical value was ≥2. Highly variable genes along the pseudotime were identified using differentialGeneTest function of Monocle2 with *q* value <0.01. Genes varying across branch points were analyzed using the BEAM function. To calculate RNA velocity of single cells, we used CellRanger 6-derived BAM files together with velocyto to generate a loom file containing the quantification of spliced and unspliced RNA. We then subsetted the matrix to randomly subsampled cells of interest using scanpy (v.1.8)[58] and calculated RNA velocity using packages velocyto (v.0.6)[59] and scvelo (v.0.2.4)[60], respectively. For velocyto, we used function RunVelocity with parameters kCells, 25 and fit.quantile, 0.02 to compute velocity. For scvelo, we used stochastic modeling of RNA velocity in function scv.tl.velocity. Results were projected onto diffusion map reduction space produced with package destiny[61].

Identification of cell–cell interaction changes. Mouse orthologs of human ligand–receptor pairs were obtained from Ensembl BioMart (http://www.ensembl.org/biomart/martview). A ligand or receptor was defined as 'expressed' in a particular cell cluster if more than 20% of the cells in the cell cluster have non-zero unique molecular identifier counts for the gene encoding the ligand or receptor.

Gene regulatory network inference. To identify transcription factors (TFs) and characterize cell states, we employed *cis*-regulatory analysis using the R package SCENIC (v.1.2.4)[62], which infers the gene regulatory network based on coexpression and DNA motif analysis. The network activity is then analyzed in each cell to identify recurrent cellular states. In short, TFs were identified using GENIE3 (v.1.12.0) and compiled into modules (regulons), which were subsequently subjected to *cis*-regulatory motif analysis using RcisTarget with two gene-motif rankings: 10 kb around the transcription start site and 500 bp upstream. Regulon activity in every cell was then scored using AUCell. Finally, binarized regulon activity was projected onto UMAP space.

Mouse bulk RNA-seq analysis. Total RNA were isolated using the RNeasy mini kit (QIAGEN). Sequencing libraries were constructed using the Illumina TruSeq RNA Preparation kit. High-throughput sequencing was performed using Illumina HiSeq4000 with 100-bp single-end according to the manufacturer's instruction. Adaptor and low-quality reads were trimmed using Trim-galore. Reads were aligned to the Gencode mouse genome (GRCm38) using STAR (v.2.4.1d). The aligned reads were mapped to the genes (GRCm38, v.7 Ensembl 82) using HTSeq-0.6.1. DEGs between sham and UUO groups were identified using DESeq2 v.1.10.1.

Human bulk gene profiling data analysis. The human study was deemed exempt by the Institutional Review Board of the University of Pennsylvanian as no personal identifiers were collected. Kidney tissues from 95 human patients (microarray) and 432 human patients (RNA-seq) were collected from the unaffected portion of surgical nephrectomies. The collected kidney was immersed into RNAlater and stored at −80 °C. Tubule compartments were manually microdissected from the tissue and subjected to RNA isolation. The rest of tissue was used for histopathological analysis. Gene expression analysis in microarray was performed using Affymetric U133A arrays (E-MTAB-2502). Raw expression levels of microarray datasets were normalized using the RMA algorithm and log transformed. Correlation analysis in RNA-seq for gene expression, fibrosis and eGFR were performed using Spearman's correlation.

Estimation of cell proportions. CIBERSORTx (https://cibersortx.stanford.edu/)[63] was used to deconvolute (determine the percent of each cell type) the bulk RNA-seq data of mouse and human kidney samples.

Histology. Kidney tissue was fixed in 10% formalin. Paraffin-embedded sections at 5-µm thick were used. H&E staining and Sirius red staining (24901, Polysciences) were performed according to manufacturer's protocol. The degree of tubulointerstitial damage was scored semi-quantitatively on a 0 to 5+ scale, according to the percentage of the area affected by hyaline casts, tubular atrophy, tubular lumen dilation and interstitial immune cells infiltration (0, normal; 1, <10%; 2, 10–25%; 3, 26–50%; 4, 51–75%; and 5, >75%). The percentage of Sirius red-positive area was quantified using ImageJ (National Institutes of Health)[64]. A total of 5–8 independent fields in kidneys from each mouse were analyzed and the mean value was plotted.

For immunofluorescence staining, sections were deparaffinized using xylene, 100% alcohol, 95 alcohol, 70% alcohol and distilled water. Epitope retrieval was performed using Tris-EDTA buffer (10 mM Tris, 1 mM EDTA solution and 0.05% Tween 20, pH 9.0) at 95 °C for 10 min. Sections were immersed in 3% H_2O_2 for blocking endogenous peroxidase for 10 min. After blocking with 10% FBS, the sections were incubated with anti-basophil (2D7) (Abcam ab155577, 1:100

dilution) at 4 °C overnight. The next day, sections were incubated with donkey anti-rabbit Alexa Fluor 555 (A-31572, Thermo Fisher, 1:500 dilution). Sections then were mounted using ProLong Gold Antifade Mounting with 4,6-diamidino-2-phenylindole (P36935, Life Sciences). Basophils were counted on 5–8 independent fields under ×200 magnification.

In situ hybridization. In situ hybridization was performed using formalin-fixed paraffin-embedded tissue samples and RNAscope 2.5 HD Duplex Detection kit (Bio-Techne, 322436). We followed the manufacturer's original protocol. The following probes were used for the RNAscope assay: Mm-*Hnf4a*-C2 497651, Mm-*Cxcl1* 407721, Mm-*Tnfrsf12a* 429311, Mm-*Bcl3* 528431, Mm-*Cd74* 37501, Mm-*Cxcl10* 408921, Mm-*Pdgfb* 424651, Mm-*Ihh* 413091 Mm-*Il18* 416731, Mm-*Il33* 400591, Mm-Mcpt8 583151, Mm-Cxcr2-CDS-C2 487671 and Mm-*Il6*-C2 315891. For quantification of the target signal in proximal renal tubules, we used a semi-quantitative histological scoring methodology based on modified ACD scoring criteria (0, no dots per cell; 1, 1–2 dots per cell; 2, 3–5 dots per cell; 3, 6–10 dots per cell; 4, >10 dots per cell and/or >20% dots per cell). We counted the dots in 20–30 renal proximal tubule cells under high power field and plotted average scores per sample.

Flow cytometry. Splenocytes were obtained by grinding spleens through a 70-µm filter and washing with RPMI supplemented with 5% FBS. Red blood cells were then lysed by incubating samples with ACK lysis buffer (Thermo Fisher Scientific) for 5 min before washing again with RPMI + 5% FBS. Cells were then washed with FACS Buffer (1× PBS, 0.2% bovine serum antigen and 1 mM EDTA) before incubating with Fc block (99.5 % FACS Buffer, 0.5% normal rat serum and 1 µg ml^{-1} 2.4G2 IgG antibody) before staining. Cells were stained with the viability dye Ghost Dye Violet 510 (Tonbo Biosciences, 12-0870) and the following antibodies were used for subsequent staining (1:200 dilution for all antibodies): B220 FITC (RA3-6B2; BioLegend), CD3e PerCP-Cy5.5 (145-2C11; Invitrogen) BV785 (17A2; BioLegend), CD4 BV650 (RM4-5; BioLegend), CD8 PE-cf594 (53-6.7; BD Biosciences), CD19 PerCP-Cy5.5 (1D3/CD19; BioLegend), CD45 AF700 and APC-e780 (30-F11; BioLegend, Invitrogen), CD49b FITC and PerCP-ef710 (DX5; BD Biosciences, eBioscience), CD117/cKit APC-e780 (ACK2; Invitrogen), CD150/SLAM BV711 (TC15-12F12.2; BioLegend), CD200R3 PE (BA13; BioLegend), CXCR5 PE-Cy7 (SPRCL5; Invitrogen), FcEr APC (MAR-1; Invitrogen), Foxp3 ef450 (FJK-16s; Invitrogen), GR1 FITC (RB6-8C5; eBioscience), Ly6G Pacific Blue (1A8; BioLegend), NK1.1 FITC and PerCP-Cy5.5 (PK136; eBioscience, BioLegend), RORγT PE (B2D; eBioscience) and Tbet BV605 (4B10; BioLegend). Intracellular staining was performed using the Foxp3/Transcription Factor Staining Buffer Set (eBioscience) according to the manufacturer's instructions. Samples were run on either a FACSCanto or LSR Fortessa (BD Biosciences) and analyzed using FlowJo (TreeStar).

In vitro basophil recruitment and activation. WT mice were injected intravenously (i.v.) with a combination of 1 µg mouse recombinant IL-3 (R&D systems) and 0.5 µg of anti-IL-3 (BioLegend, clone MP2-8F8) in 200 µl of PBS 3 d before being killed. Single-cell suspensions from spleens were prepared and basophils were sort-purified as CD45$^+$, CD3$^-$, CD19$^-$, NK1.1$^-$, Ly6G$^-$, Siglec-F$^-$, cKit$^-$, CD49b$^+$ and CD200R$^+$ cells using a FACSAriaII (BD Bioscience). Siglec-F was used to exclude eosinophils. Purity for all cell populations were determined to be 98% or greater. The gating strategy and cytology is shown in Supplementary Fig. 7a,b. For the chemotaxis assay, 30,000 cells were treated with 10 nM CXCL1 for 2 h. The recruited basophils were assessed according to manufacturer's protocol (Cell Biolabs, CBA-105). For basophil activation, basophils were resuspended in 200 µl of culture medium and stimulated with 10 ng ml^{-1} rIL-18 or rIL-33 (R&D Systems) in the absence of IL-3 overnight and cell-free supernatant were evaluated for IL-6 by standard ELISA. Cells were stained with monoclonal anti-mouse fluorescently conjugated antibodies: CD45 (30-F11), CD3 (145-2C11), CD19 (1D3), NK1.1 (PK136), Ly6G (1A8), Siglec-F (E50-2440), cKit (2b8), CD200R1 (OX110), CD200R3 (Ba13) and CD49b (DX5) from eBioscience or BD Biosciences.

IL-6 quantification in kidney tissue. Kidney tissue was homogenized in RIPA buffer containing proteinase inhibitor. After 10 min centrifugation at 4 °C, tissue lysates were used for IL-6 measurement according to manufacturer's protocol (M6000B, R and D Mouse IL-6 Immunoassay). The IL-6 data were corrected for total protein levels measured by Pierce BCA Protein Assay kit (23225, Thermo Fisher).

Real-time quantitative PCR. Sham and UUO kidneys were homogenized and total RNA were extracted using Trizol, according to manufacturer's protocol (Thermo Fisher). Quality and concentration of extracted RNA were examined using nanodrop. Complementary DNA was generated using Reverse Transcription kit (Applied Biosystems) according to the manufacturer's protocol. Real-time quantitative PCR were performed using Cyber green Master Mix Reagents (Thermo Fisher) with ViiA 7 System (Life Technologies) instrument. Primer sequences are listed in Supplementary Table 8.

Data statistics and analysis. The data were expressed as mean ± s.e.m. Statistical significance was assessed by a two-tailed Student's *t*-test for two-group comparisons or a one-way ANOVA for multigroup comparisons followed by Tukey post hoc test for subgroup comparisons. $P < 0.05$ was considered significant. Data distribution was assumed to be normal but this was not formally tested. Data collection and analysis were not performed blind to the conditions of the experiments. No data exclusion was performed. The clipart in the figure was created using images from Smart Servier Medical Art (https://smart.servier.com/).

Reporting Summary. Further information on research design is available in the Nature Research Reporting Summary linked to this article.

Data availability

The mouse UUO single-cell data presented in this paper are newly deposited to GSE182256. The publicly available mouse UUO single-cell data were obtained from GSE140023. The human kidney gene expression data can be downloaded from GSE173343, GSE115098. GRCm38 and GRCh38 were used for mice and human reference genome assembly, respectively.

Code availability

The code is available at GitHub (https://github.com/ms-balzer/kidney_basophils).

References

53. Doke, T. et al. Transcriptome-wide association analysis identifies DACH1 as a kidney disease risk gene that contributes to fibrosis. *J. Clin. Invest.* https://doi.org/10.1172/JCI141801 (2021).
54. Hao, Y. et al. Integrated analysis of multimodal single-cell data. *Cell* **184**, 3573–3587 (2021).
55. Korsunsky, I. et al. Fast, sensitive and accurate integration of single-cell data with Harmony. *Nat. Methods* **16**, 1289–1296 (2019).
56. McGinnis, C. S., Murrow, L. M. & Gartner, Z. J. DoubletFinder: doublet detection in single-cell RNA sequencing data using artificial nearest neighbors. *Cell Syst.* **8**, 329–337 (2019).
57. Qiu, X. et al. Reversed graph embedding resolves complex single-cell trajectories. *Nat. Methods* **14**, 979–982 (2017).
58. Wolf, F. A., Angerer, P. & Theis, F. J. SCANPY: large-scale single-cell gene expression data analysis. *Genome Biol.* **19**, 15 (2018).
59. La Manno, G. et al. RNA velocity of single cells. *Nature* **560**, 494–498 (2018).
60. Bergen, V., Lange, M., Peidli, S., Wolf, F. A. & Theis, F. J. Generalizing RNA velocity to transient cell states through dynamical modeling. *Nat. Biotechnol.* **38**, 1408–1414 (2020).
61. Angerer, P. et al. Destiny: diffusion maps for large-scale single-cell data in R. *Bioinforma.* **32**, 1241–1243 (2016).
62. Aibar, S. et al. SCENIC: single-cell regulatory network inference and clustering. *Nat. Methods* **14**, 1083–1086 (2017).
63. Steen, C. B., Liu, C. L., Alizadeh, A. A. & Newman, A. M. Profiling cell type abundance and expression in bulk tissues with CIBERSORTx. *Methods Mol. Biol.* **2117**, 135–157 (2020).
64. Schindelin, J. et al. Fiji: an open-source platform for biological-image analysis. *Nat. Methods* **9**, 676–682 (2012).

Acknowledgements

This work has been supported in the Susztak laboratory by the National Institutes of Health R01 DK087635, DK076077 and DK105821 and in the Lefebvre laboratory by the National Institutes of Health NIAMS R01 grant AR068308. M.S.B. is supported by a German Research Foundation (Deutsche Forschungsgemeinschaft) grant (BA 6205/2-1). The authors thank the Molecular Pathology and Imaging Core (P30-DK050306) and Diabetes Research Center (P30-DK19525) at University of Pennsylvania for their services.

Author contributions

T.D., D.A.A., Y.Y., C.M.H. and R.S. performed experiments and analyzed data. J.P., A.A., M.S.B. and S.X. performed computational analysis. G.C., J.I.R., S.H. and J.K. offered experimental suggestion. A.P., M.A. and V.L. provided resources and advice. K.S. was responsible for overall design and oversight of the experiments. M.C.S., C.A.H. and K.S. supervised the experiment. T.D., J.P. and K.S. wrote the original draft. All authors contributed to and approved the final version of the manuscript.

Competing interests

The authors declare no competing interests.

Additional information

Extended data is available for this paper at https://doi.org/10.1038/s41590-022-01200-7.

Supplementary information The online version contains supplementary material available at https://doi.org/10.1038/s41590-022-01200-7.

Correspondence and requests for materials should be addressed to Katalin Susztak.

Peer review information *Nature Immunology* thanks Matthias Mack and the other, anonymous, reviewer(s) for their contribution to the peer review of this work. Primary Handling Editor: Nicholas Bernard, in collaboration with the *Nature Immunology* team. Peer reviewer reports are available.

Reprints and permissions information is available at www.nature.com/reprints.

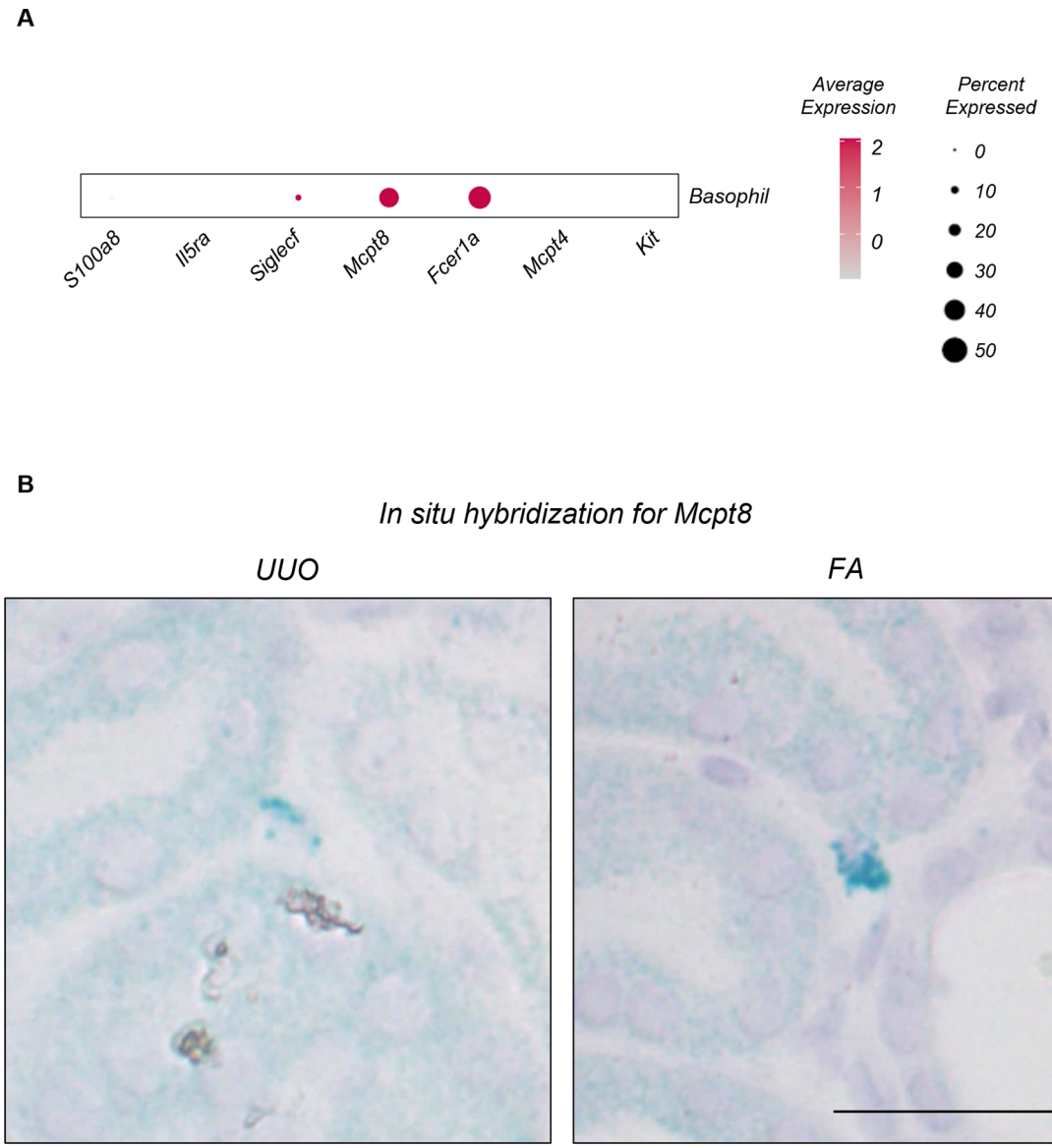

Extended Data Fig. 1 | *Mcpt8* expression in basophils in kidney fibrosis. (**A**) Bubble plots showing the average gene expression and percentage of expressing cells of *S100a8, Il5ra, Siglecf, Mcpt8, Fcer1a, Mcpt4* and *kit* in the basophils. (**B**) Representative in situ hybridization image of *Mcpt8* in kidney fibrosis following UUO or injection of folic acid. Scale bar: 50 μm. Data are representative of two independent experiments.

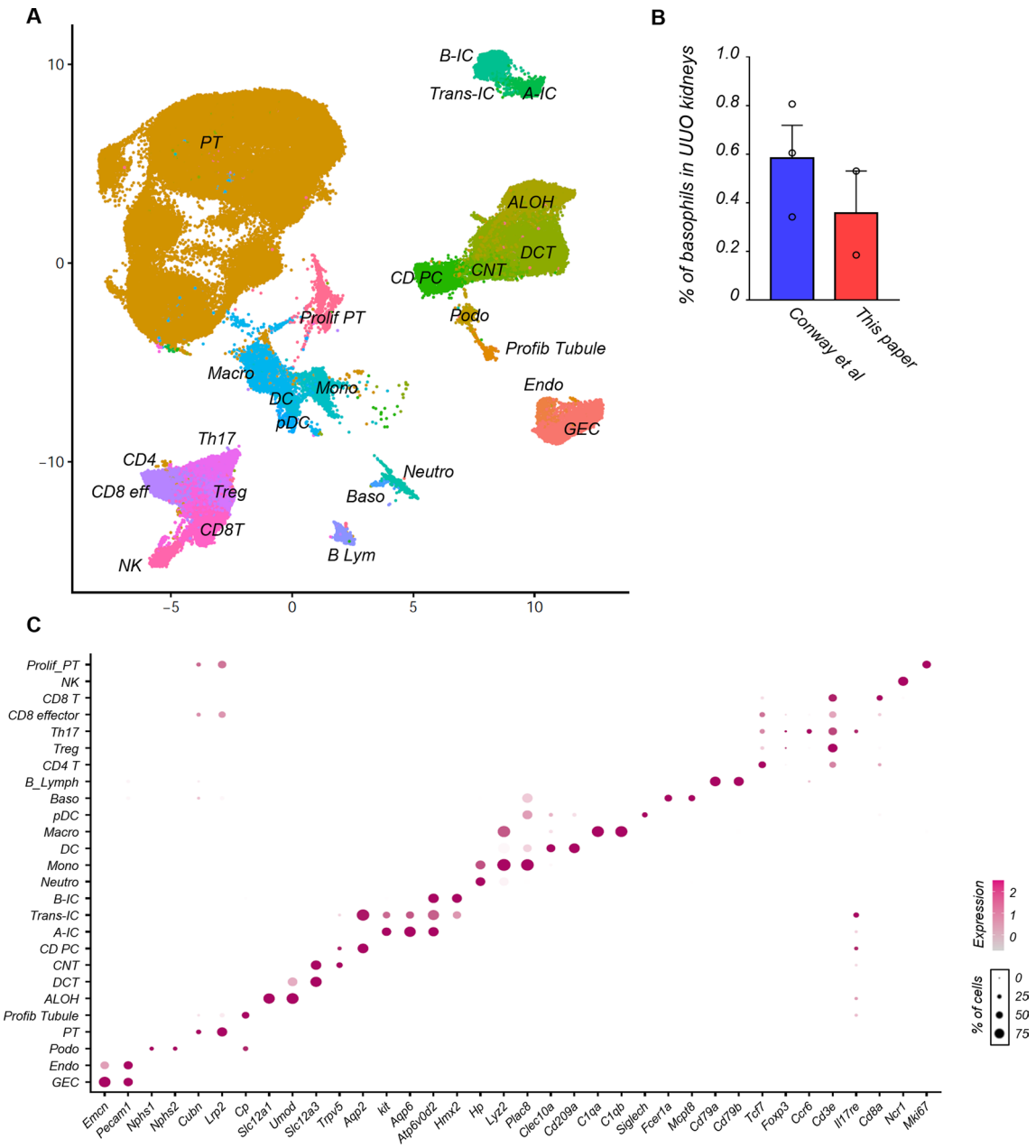

Extended Data Fig. 2 | Integration analysis using published dataset. (**a**) UMAP dimension reduction showing 26 distinct cell types identified by unsupervised clustering. Sample number, Sham; n = 7, UUO; n = 5. GEC: glomerular endothelial cells, Endo: endothelial, Podo: podocyte, PT: proximal tubule, ALOH: ascending loop of Henle, DCT: distal convoluted tubule, CNT: connecting tubule, CD PC: collecting duct principal cell, A-IC: alpha intercalated cell, B-IC: beta intercalated cell, Trans-IC: transitional intercalated cell, Neutro: Neutrophils, Mono: monocyte, DC: dendritic cell, Macro: macrophage, pDC: plasmacytoid DC, Baso: Basophile B Lymph: B lymphocyte, NK: natural killer cell. (**b**) The percentage of basophils detected in single-cell RNA-seq in UUO kidneys. n = 3 from the published database (Conway et al), n = 2 from this paper. Data are presented as mean values ± SEM. (**c**) Bubble plots showing the expression of cell cluster marker genes in the combined dataset.

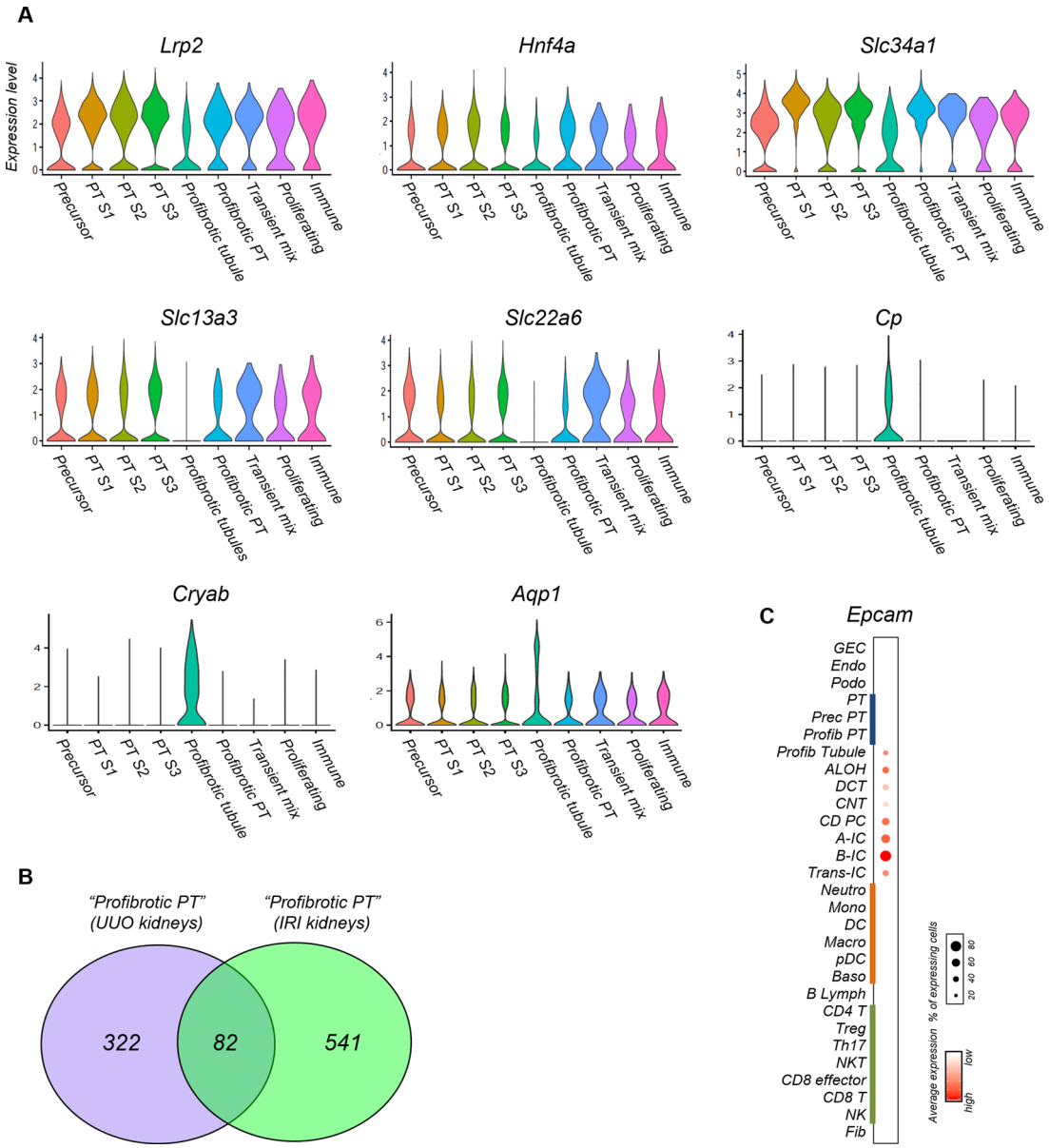

Extended Data Fig. 3 | Marker gene expressions of renal tubule cells in UUO kidneys. (**a**) Violin plots showing the average expression and percentage of cells expressing *Lrp2, Hnf4a, Slc34a1, Slc13a3, Slc22a6, Cp, Cryab*, and *Aqp1* in the PT subcluster in UUO kidneys. (**b**) Venn diagram of differentially expression genes in profibrotic proximal renal tubules in UUO kidneys and ischemia reperfusion injury (IRI) kidneys. (**c**) Bubble plots showing the average expression and percentage of cells expressing *Epcam* in UUO kidneys.

Extended Data Fig. 4 | SCENIC regulon activity of PT clusters in UUO kidneys. (Left panel) Heat map of predicted transcription factor activity in PT subclusters (Precursor, S2, S3, Transient mix, Proliferating, Immune, S1, and Profibrotic PT). Red indicates higher regulon activity, blue indicates lower regulon activity. (Right panel) Feature plots of the regulon activity (AUC) for representative transcription factors of *Bcl3*, *Cebpb*, *Stat3*, *Klf6*, *Stat5a*, and *Ddit3*.

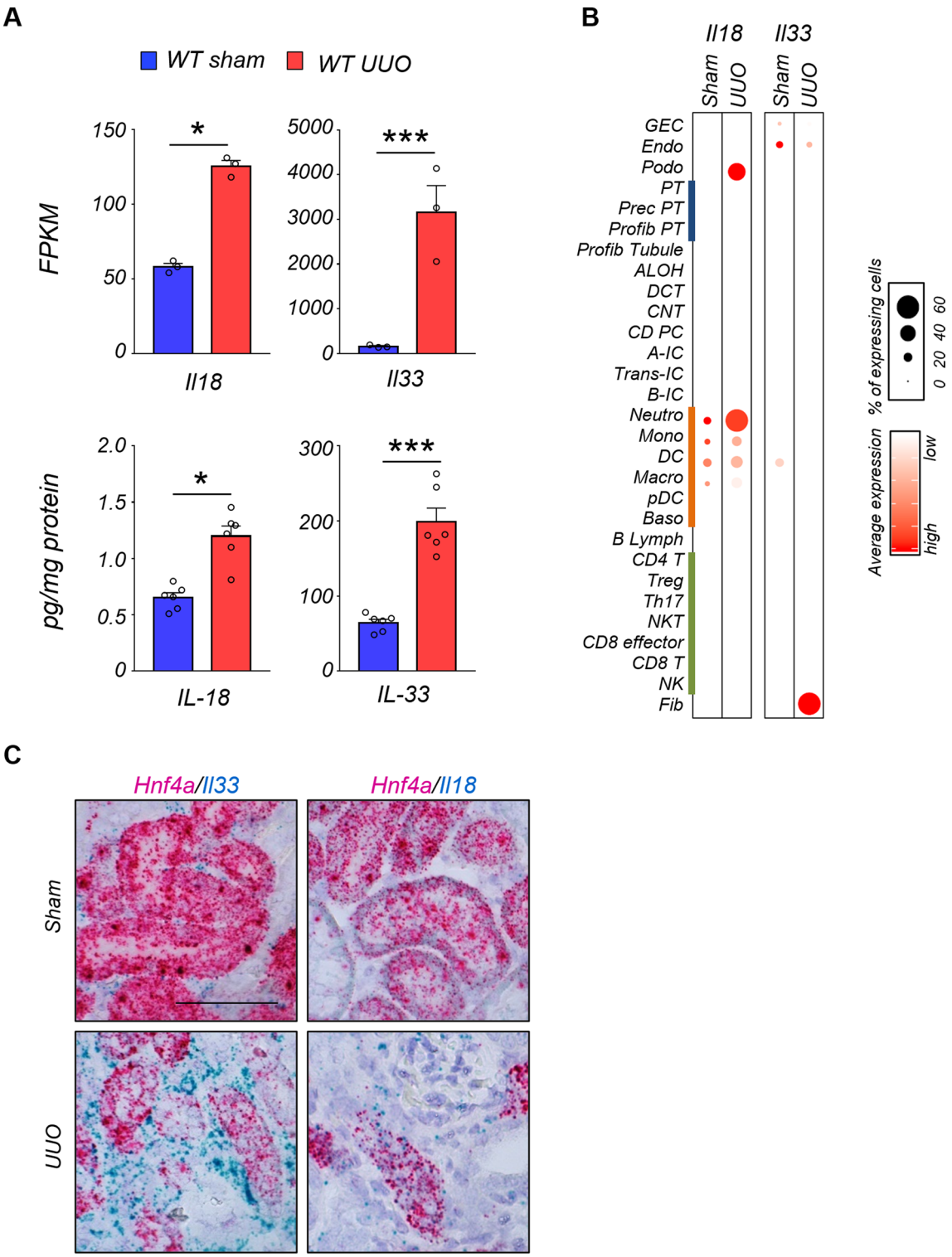

Extended Data Fig. 5 | The expression levels of *Il18*, *Il33* in UUO kidneys. (**a**) Whole kidney gene and protein expression levels in sham and UUO kidneys of wild-type (WT) mice (n = 3 respectively). (**b**) Bubble plots showing the average gene expression and percentage of expressing cells of *Il18* and *Il33* in sham and UUO kidneys. Gene expression levels are shown as FPKM values (quantified by RNA-seq) and protein levels (quantified by ELISA) are corrected with total protein levels. *$p < 0.05$, ***$p < 0.001$. Data are presented as mean values ± SEM. Data were analyzed using DEseq2. (**c**) The representative image of in situ hybridization of *Il18* and *Il33* with *Hnf4a* in sham and UUO kidneys. Scale bar; 20 μm. Data are representative of two independent experiments.

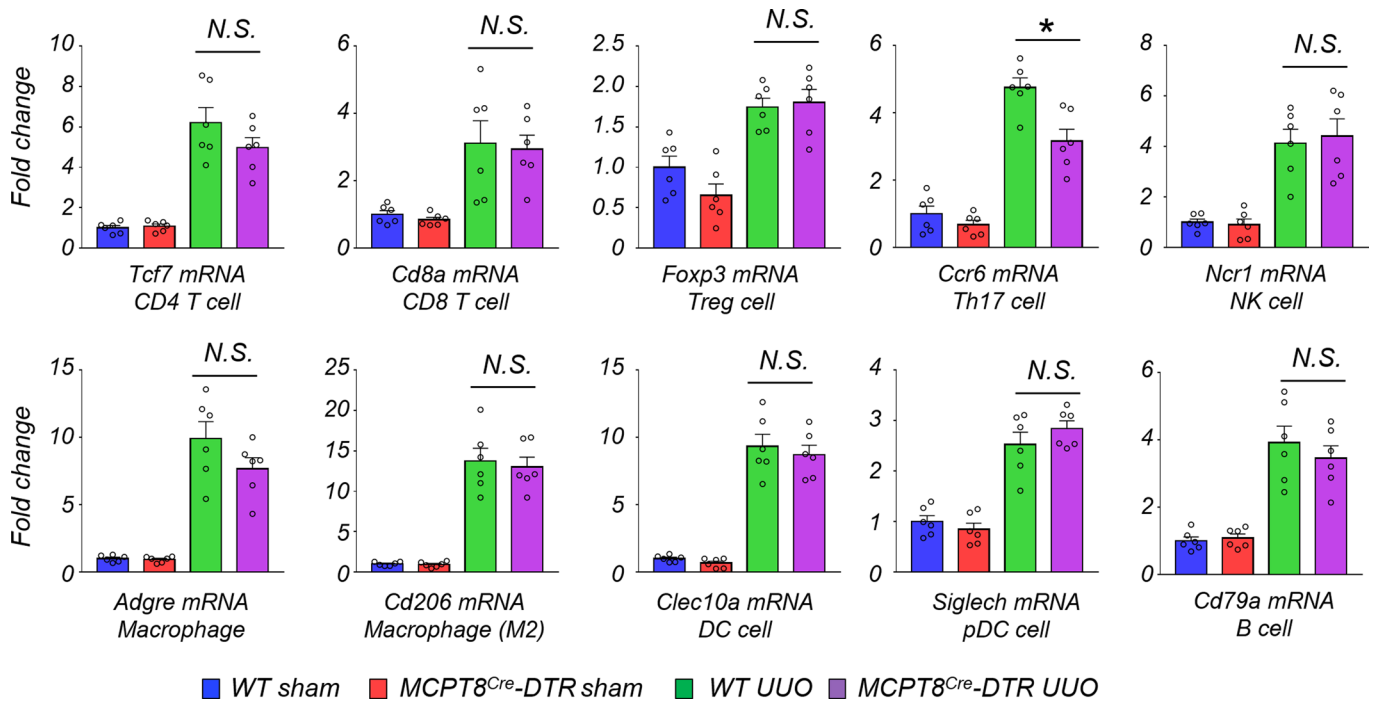

Extended Data Fig. 6 | Immune cell survey of MCPT8Cre-DTR mice kidneys. Relative transcript level of immune cell markers *Tcf7, Cd8a, Foxp3, Ccr6, Ncr1, Cd79a, Adgre, Cd206, Clec10a*, and *Siglech* in kidneys of experimental groups (n = 6 in each group). Gene expression levels in whole kidney samples were normalized to Gapdh. *$p < 0.05$. N.S. not significant. Data are presented as mean values ± SEM. All data were analyzed using a one-way ANOVA followed by Tukey post hoc test for multigroup comparison.

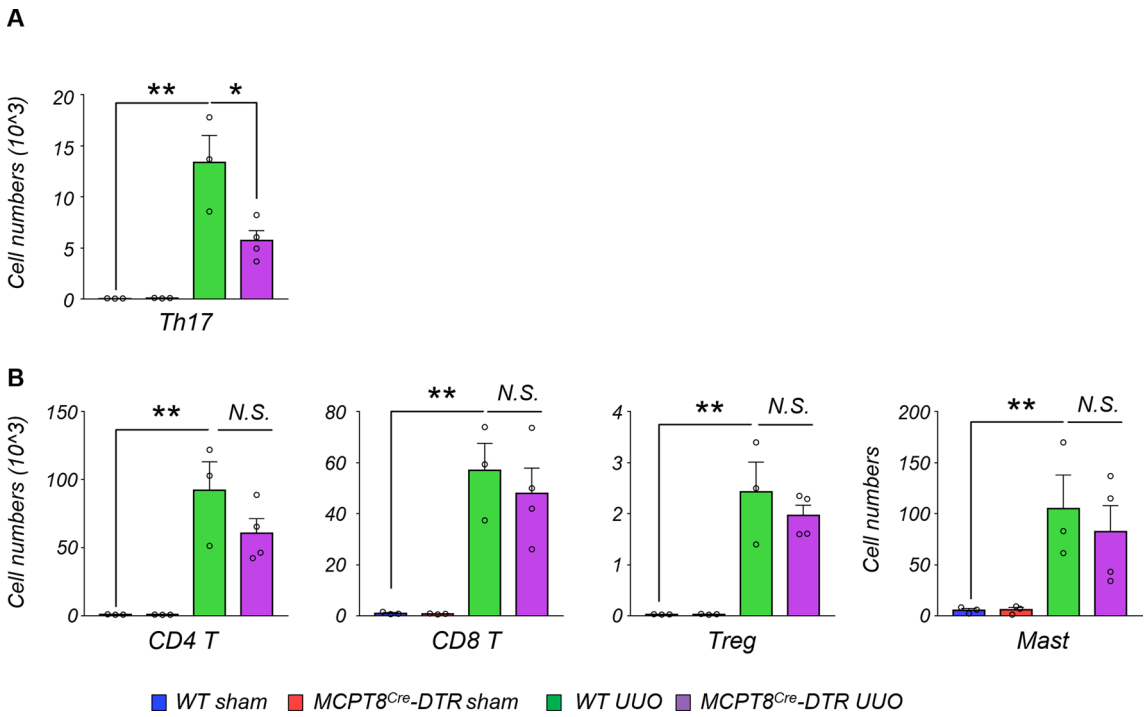

Extended Data Fig. 7 | Changes in immune cell population in kidneys of Mcpt8^{cre}-DTR mice. (**a**) The number of Th17 cells in kidneys of experimental groups identified by FACS (n = 3 in WT sham, MCPT8Cre-DTR sham, and WT UUO. n = 4 in MCPT8Cre-DTR UUO). *p < 0.05, **p < 0.01. (**b**) The number of CD4, CD8, Treg, and mast cells in kidneys of experimental groups identified by flow sorting (n = 3 in WT sham, MCPT8Cre-DTR sham, and WT UUO. n = 4 in MCPT8Cre-DTR UUO). **p < 0.01. N.S. not significant. (**a**-**b**) Data are presented as mean values ± SEM. All data were analyzed using a one-way ANOVA followed by Tukey post hoc test for multigroup comparison.

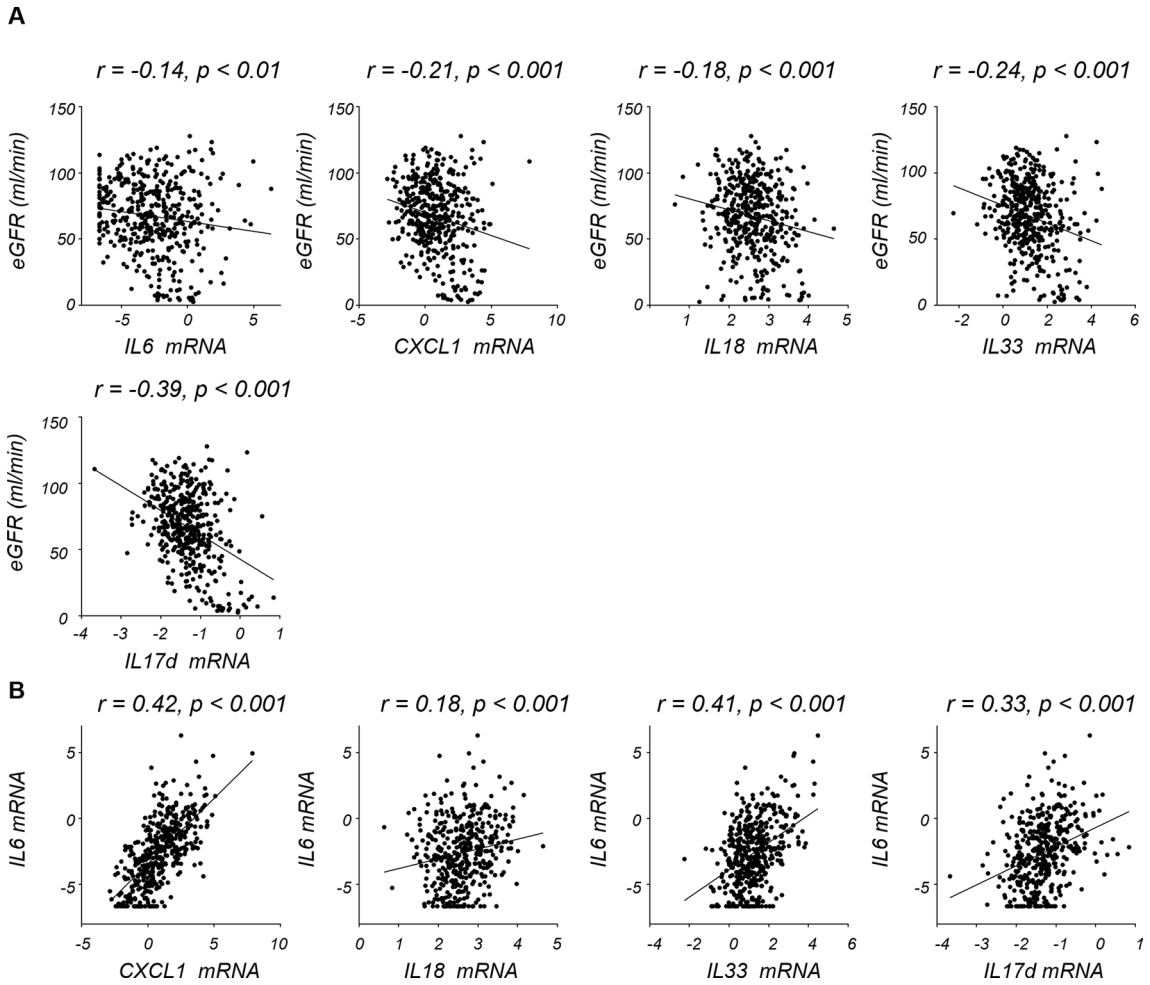

Extended Data Fig. 8 | Gene expression correlation in microdissected human kidney tubule samples. (**a**) Correlation between *IL6*, *CXCL1*, *IL18*, *IL33*, *IL17d* normalized expression levels in human kidney samples (x axis) and eGFR (ml/min) (y axis). (**b**) Correlation between *CXCL1*, *IL18*, *IL33*, *IL17d* normalized expression levels (x axis) and *IL6* normalized expression levels (y axis) in human kidney samples. Pearson's correlation coefficient values are shown.

nature portfolio

Corresponding author(s): Katalin Susztak

Last updated by author(s): Mar 4, 2022

Reporting Summary

Nature Portfolio wishes to improve the reproducibility of the work that we publish. This form provides structure for consistency and transparency in reporting. For further information on Nature Portfolio policies, see our Editorial Policies and the Editorial Policy Checklist.

Statistics

For all statistical analyses, confirm that the following items are present in the figure legend, table legend, main text, or Methods section.

n/a	Confirmed
☐	☒ The exact sample size (*n*) for each experimental group/condition, given as a discrete number and unit of measurement
☐	☒ A statement on whether measurements were taken from distinct samples or whether the same sample was measured repeatedly
☐	☒ The statistical test(s) used AND whether they are one- or two-sided *Only common tests should be described solely by name; describe more complex techniques in the Methods section.*
☐	☒ A description of all covariates tested
☐	☒ A description of any assumptions or corrections, such as tests of normality and adjustment for multiple comparisons
☐	☒ A full description of the statistical parameters including central tendency (e.g. means) or other basic estimates (e.g. regression coefficient) AND variation (e.g. standard deviation) or associated estimates of uncertainty (e.g. confidence intervals)
☐	☒ For null hypothesis testing, the test statistic (e.g. *F*, *t*, *r*) with confidence intervals, effect sizes, degrees of freedom and *P* value noted *Give P values as exact values whenever suitable.*
☒	☐ For Bayesian analysis, information on the choice of priors and Markov chain Monte Carlo settings
☒	☐ For hierarchical and complex designs, identification of the appropriate level for tests and full reporting of outcomes
☐	☒ Estimates of effect sizes (e.g. Cohen's *d*, Pearson's *r*), indicating how they were calculated

Our web collection on statistics for biologists contains articles on many of the points above.

Software and code

Policy information about availability of computer code

Data collection	Cell Ranger v6.0.1 (http://10xgenomics.com) was used to process Chromium single cell 3' RNA-seq output.
Data analysis	Seurat R package (version 4.0.3) was used for snRNA-seq matrix generation, clustering, and finding cell type specific genes. To remove the batch effect, Harmony (v1.0) was used. Doublet-like cells were identified using DoubletFinder (v2.0.3). To construct the single-cell pseudotime trajectory, the Monocle2 (version 2.4.0) algorithm was applied to proximal tubule and immune cells. To calculate RNA velocity of single cells, we used CellRanger 6-derived BAM files together. We then subset the matrix to randomly subsampled cells of interest using scanpy (v1.8) and calculated RNA velocity using packages velocyto (v0.6) and scvelo (v0.2.4), respectively. To identify TFs and characterize cell states, we employed cis-regulatory analysis using the R package SCENIC (v1.2.4). TFs were identified using GENIE3 (v1.12.0). For the mice bulk RNS-seq, we used STAR(v2.4.1d), HTSeq-0.6.1 for data processing, and used DESeq2 to detect differentially expressed genes. CIBERSORTx (https://cibersortx.stanford.edu/) was used to deconvolute the bulk RNA sequencing data of mice and human kidney samples. Mouse orthologs of human ligand-receptor pairs were obtained from Ensembl BioMart. Samples of flow cytometry were run on either a FACSCanto or LSR Fortessa (BD Biosciences) and analyzed using the FlowJo Software analysis program (TreeStar). Real time quantitative PCR were performed using Cyber green Master Mix Reagents (Thermo Fisher) with ViiA 7 System (Life Technologies) instrument. The code is available at GitHub (https://github.com/ms-balzer/kidney_basophils).

For manuscripts utilizing custom algorithms or software that are central to the research but not yet described in published literature, software must be made available to editors and reviewers. We strongly encourage code deposition in a community repository (e.g. GitHub). See the Nature Portfolio guidelines for submitting code & software for further information.

Data

Policy information about availability of data

All manuscripts must include a data availability statement. This statement should provide the following information, where applicable:

- Accession codes, unique identifiers, or web links for publicly available datasets
- A description of any restrictions on data availability
- For clinical datasets or third party data, please ensure that the statement adheres to our policy

The mouse single-cell data are deposited in GSE182256 and GSE140023. The human kidney gene expression data can be downloaded from GSE173343, GSE115098. GRCm38 and GRCh38 were used for mice and human reference genome assembly respectively.

Field-specific reporting

Please select the one below that is the best fit for your research. If you are not sure, read the appropriate sections before making your selection.

☒ Life sciences ☐ Behavioural & social sciences ☐ Ecological, evolutionary & environmental sciences

For a reference copy of the document with all sections, see nature.com/documents/nr-reporting-summary-flat.pdf

Life sciences study design

All studies must disclose on these points even when the disclosure is negative.

Sample size	No statistical methods were used to predetermine sample sizes. The sample size for animal study was more than 3 mice per group.
Data exclusions	No data were excluded from mice experiments
Replication	All the experiments were successfully replicated at least two times. The sample numbers and independent experiment numbers were shown in figure legends. scRNA sequence were performed once while we confirmed our result using a public available database.
Randomization	Randomization was not relevant to this study. Mice were grouped by genotype.
Blinding	The samples were not blinded to the authors. All the experiments were objective and the conclusion were based on independent experiments, multiple technical replicates, and statistics significance. The information of the kidney function of human samples and genotype of mice samples were known when we analyzed the data.

Reporting for specific materials, systems and methods

We require information from authors about some types of materials, experimental systems and methods used in many studies. Here, indicate whether each material, system or method listed is relevant to your study. If you are not sure if a list item applies to your research, read the appropriate section before selecting a response.

Materials & experimental systems

n/a	Involved in the study
☐	☒ Antibodies
☒	☐ Eukaryotic cell lines
☒	☐ Palaeontology and archaeology
☐	☒ Animals and other organisms
☐	☒ Human research participants
☒	☐ Clinical data
☒	☐ Dual use research of concern

Methods

n/a	Involved in the study
☒	☐ ChIP-seq
☐	☒ Flow cytometry
☒	☐ MRI-based neuroimaging

Antibodies

Antibodies used

The following antibodies were used for flow cytometry (all 1:200 dilution):
B220 FITC (RA3-6B2; BioLegend),
CD3e PerCP-Cy5.5 (145-2C11; Invitrogen)
BV785 (17A2; BioLegend),
CD4 BV650 (RM4-5; BioLegend),
CD8 PE-cf594 (53-6.7; BD Biosciences),
CD19 PerCP-Cy5.5 (1D3/CD19; BioLegend),
CD45 AF700 and APC-e780 (30-F11; BioLegend, Invitrogen),
CD49b FITC and PerCP-ef710 (DX5; BD Biosciences, eBioscience),

CD117/cKit APC-e780 (ACK2; Invitrogen),
CD150/SLAM BV711 (TC15-12F12.2; BioLegend),
CD200R3 PE (BA13; BioLegend), CXCR5 PE-Cy7 (SPRCL5; Invitrogen),
FcEr APC (MAR-1; Invitrogen), Foxp3 ef450 (FJK-16s; Invitrogen),
GR1 FITC (RB6-8C5; eBioscience),
Ly6G Pacific Blue (1A8; BioLegend),
NK1.1 FITC and PerCP-Cy5.5 (PK136; eBioscience, BioLegend),
RORγT PE (B2D; eBioscience),
Tbet BV605 (4B10; BioLegend).
CD45 (30-F11,eBioscience),
CD3 (145-2C11,eBioscience),
CD19 (1D3,eBioscience),
NK1.1 (PK136,eBioscience),
Ly6G (1A8,eBioscience),
Siglec-F (E50-2440,eBioscience),
c-Kit (2b8,eBioscience),
CD200R1 (OX110,eBioscience),
CD200R3 (Ba13,eBioscience),
CD49b (DX5,eBioscience)

The following antibodies were used for immunofluorescence.
anti-Basophils antibody [2D7] (#ab155577,abcam,1:200)
Donkey anti-Rabbit Alexa fluor 555 (Thermo fisher, 1:500).

The following antibodies were used for in vivo mice experiments. The dose and timing were described in the method section.
Armenian anti-mouse FcεRIα antibody (# 16-5898-85, clone;MAR-1, eBioscience) and isotype control IgG antibody (Armenian hamster IgG, eBioscience ((#16-4888-85, Armenian hamster IgG, eBioscience)
anti-IL-6R Ab (#BE0047, clone 15A7; BioXCell) and isotype control IgG (#BE0090 , BioXCell)

Validation

All commercially available antibodies listed above were validated by manufacturers as documented on the website of the companies.

Animals and other organisms

Policy information about studies involving animals; ARRIVE guidelines recommended for reporting animal research

Laboratory animals	All mouse experiments were performed between 8 to 12 weeks. We used C57BL/6 genetic background mice and mice were housed under Specific Pathogen Free (SPF) conditions with a 12 hour dark/light cycle, 22–25 °C, and 50-60% humidity with water and food provided ad libitum. DTR mice were purchased from the Jackson laboratory (Stock No: 009669).
Wild animals	No wild animals were used.
Field-collected samples	the study did not involve samples collected from the field.
Ethics oversight	Animal studies were approved by the Institutional Animal Care and Use Committee (IACUC) of the University of Pennsylvania.

Note that full information on the approval of the study protocol must also be provided in the manuscript.

Human research participants

Policy information about studies involving human research participants

Population characteristics	The population characteristic of adult human kidney samples for microarray and RNA-seq were described in the supplementary table 7 and 8. The datasets include the information about gender, ethnicity, background history (BMI, Hypertension, Diabetes), renal function (serum creatinine, BUN, serum glucose, blood pressure, eGFR, histological score) and CKD stages.
Recruitment	Kidney samples were obtained from surgical nephrectomies approved by the University of Pennsylvania Institutional Review Board. Nephrectomies were de-identified, and the corresponding clinical information was collected through an honest broker. There was no selection bias.
Ethics oversight	The human study was deemed exempt by the institutional review board (IRB) of the University of Pennsylvania. Therefore, informed consent was not obtained by participants and there was no participant compensation.

Note that full information on the approval of the study protocol must also be provided in the manuscript.

Flow Cytometry

Plots

Confirm that:

☒ The axis labels state the marker and fluorochrome used (e.g. CD4-FITC).

☒ The axis scales are clearly visible. Include numbers along axes only for bottom left plot of group (a 'group' is an analysis of identical markers).

☒ All plots are contour plots with outliers or pseudocolor plots.

☒ A numerical value for number of cells or percentage (with statistics) is provided.

Methodology

Sample preparation	Splenocytes were obtained by grinding spleens through a 70 µm filter and washing with RPMI supplemented with 5% fetal bovine serum (FBS). Red blood cells were then lysed by incubating samples with ACK lysis buffer (Thermo Fischer Scientific) for 5 minutes before washing again with RPMI + 5% FBS. Cells were then washed with FACS Buffer [1x PBS, 0.2% bovine serum antigen, 1mM EDTA] before incubating with Fc block [99.5 % FACS Buffer, 0.5% normal rat serum, 1 µg/ml 2.4G2 IgG antibody] prior to staining.
Instrument	Samples were run on either a FACSCanto or LSR Fortessa (BD Biosciences)
Software	Samples were analyzed using the FlowJo Software analysis program (TreeStar)
Cell population abundance	We used established basophils sorting procedure.
Gating strategy	Basophils were sort-purified as CD45+, CD3-, CD19-, NK1.1-, Ly6G-, Siglec-F-, c-Kit-, CD49b+, CD200R+ cells using a FACSAriaII (BD Bioscience). Siglec-F was used to exclude eosinophils. Purity for all cell populations were determined to be 98% or greater.

☒ Tick this box to confirm that a figure exemplifying the gating strategy is provided in the Supplementary Information.